

UNCLASSIFIED

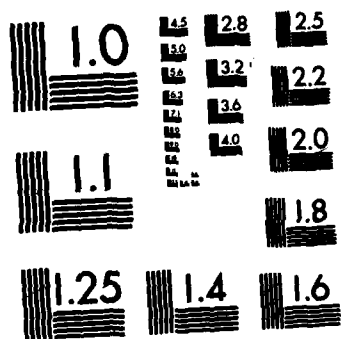
F/G 4/1

NL

END

131MFO

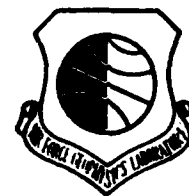
DTIC



MICROCOPY RESOLUTION TEST CHART
NATIONAL BUREAU OF STANDARDS-1963-A

ADA 124291

AFGL-TR-82-0222
ENVIRONMENTAL RESEARCH PAPERS, NO. 787



Phase and Amplitude Scintillation Statistics at 244 MHz From Goose Bay Using a Geostationary Satellite

SUNANDA BASU
SANTIMAY BASU
ROBERT C. LIVINGSTON
EILEEN MacKENZIE
HERBERT E. WHITNEY

6 August 1982

DTIC

FEB 10 1983

Approved for public release; distribution unlimited.

This work was partially sponsored by the Defense Nuclear Agency, Subtask
125AAXHX, the Space Division, Project 2029 under Contract F19628-81-
K-0011 and the AFGL In-House Laboratory Independent Research Fund.

DMC FILE COPY

SPACE PHYSICS DIVISION
AIR FORCE GEOPHYSICS LABORATORY
HANSCOM AFB, MASSACHUSETTS 01731

PROJECT 4643

AIR FORCE SYSTEMS COMMAND, USAF



89 02 010 056

This report has been reviewed by the ESD Public Affairs Office (PA)
and is releasable to the National Technical Information Service (NTIS).

This technical report has been reviewed and
is approved for publication.


DR. ALVA T. STAIR, Jr.
Chief Scientist

Qualified requestors may obtain additional copies from the
Defense Technical Information Center. All others should apply
to the National Technical Information Service.

Unclassified

SECURITY CLASSIFICATION OF THIS PAGE (When Data Entered)

REPORT DOCUMENTATION PAGE		READ INSTRUCTIONS BEFORE COMPLETING FORM
1. REPORT NUMBER AFGL-TR-82-0222	2. GOVT ACCESSION NO. AD-A124 241	3. RECIPIENT'S CATALOG NUMBER
4. TITLE (and Subtitle) PHASE AND AMPLITUDE SCINTILLATION STATISTICS AT 244 MHz FROM GOOSE BAY USING A GEOSTATIONARY SATELLITE		5. TYPE OF REPORT & PERIOD COVERED Scientific. Interim.
		6. PERFORMING ORG. REPORT NUMBER ERP No. 787
7. AUTHOR(s) Sunanda Basu * Santimay Basu * Robert C. Livingston ** Eileen MacKenzie * Herbert E. Whitney		8. CONTRACT OR GRANT NUMBER(s)
9. PERFORMING ORGANIZATION NAME AND ADDRESS Air Force Geophysics Laboratory (PHY) Hanscom AFB Massachusetts 01731		10. PROGRAM ELEMENT, PROJECT, TASK AREA & WORK UNIT NUMBERS 62101F 46430505
11. CONTROLLING OFFICE NAME AND ADDRESS Air Force Geophysics Laboratory (PHY) Hanscom AFB Massachusetts 01731		12. REPORT DATE 6 August 1982
14. MONITORING AGENCY NAME & ADDRESS (if different from Controlling Office)		13. NUMBER OF PAGES 62
		15. SECURITY CLASS. (of this report) Unclassified
		15a. DECLASSIFICATION/DOWNGRADING SCHEDULE
16. DISTRIBUTION STATEMENT (of this Report) Approved for public release; distribution unlimited.		
17. DISTRIBUTION STATEMENT (of the abstract entered in Block 20, if different from Report)		
18. SUPPLEMENTARY NOTES This work was partially sponsored by the Defense Nuclear Agency, Subtask I25AAXHX, the Space Division, Project 2029 under Contract F19628-81-K-0011 and the AFGL Laboratory Director's Fund. *Emmanuel College, Boston, MA; **SRI International, Menlo Park, CA		
19. KEY WORDS (Continue on reverse side if necessary and identify by block number) Amplitude scintillation Auroral region Particle precipitation Phase scintillation Atlantic sector F-region irregularities Magnetic index High-latitude irregularities Ionospheric scintillation statistics Signal statistics Geostationary satellite		
20. ABSTRACT (Continue on reverse side if necessary and identify by block number) Phase and amplitude scintillation measurements made at 244 MHz from Goose Bay using the geostationary satellite Fleetsat are presented. An ex- tended dynamic range receiver with an extremely stable local oscillator measured the phase variations with the precision of a coherent system subject to certain limitations. The data were obtained for a 10-month period in 1979 during a high sunspot epoch to extend the limited temporal coverage of the orbiting Wideband satellite data, reported in AFGL-TR-81-0285. The report presents scintillation statistics in the manner required for communications		

DD FORM 1 JAN 73 1473

Unclassified

SECURITY CLASSIFICATION OF THIS PAGE (When Data Entered)

Unclassified

SECURITY CLASSIFICATION OF THIS PAGE(When Data Entered)

20. (contd)

Car 1 → system planning. The nighttime phase scintillations showed maximum occurrence during the spring and increased greatly in relation to the amplitude scintillations during times of significant magnetic activity. The increase of phase scintillations in relation to amplitude scintillations was attributed to an enhanced ionospheric drift during times of magnetic disturbances. The phase spectral index p of the Fleetsat data was found to be larger than that determined from Wideband data. To further our understanding of auroral irregularity generation mechanisms, this report also presents a case study ~~the first of its kind~~ of energetic particle precipitation spectra, the topside thermal density response of such precipitation and the coordinated phase and amplitude perturbation spectra created by such an energy input into the ionosphere. The results of this case study are encouraging enough to warrant a more extensive statistical investigation into the geophysical conditions that cause such low energy electron precipitation and create associated propagation disturbances in the high latitude ionosphere.

Unclassified

SECURITY CLASSIFICATION OF THIS PAGE(When Data Entered)

Preface

This report was made possible by the contributions of many individuals and organizations. M. D. Cousins of SRI International was responsible for instrumentation and installation; Canadian Marconi Company for running the Goose Bay observational program; and N. Scotti of Bedford Research Associates for computer analysis.

We also acknowledge the assistance of D. A. Hardy in providing us with the DMSP/F2 energetic electron data and for useful discussions on its interpretation. The DMSP/F2 thermal sensor data was kindly made available by F. J. Rich and the ATS-5 polarimeter data by J. A. Klobuchar. The suitability of the 29 March 1979 data for detailed study was first pointed out by Zwi Houminer. The ISEE-3 interplanetary magnetic field data used in this report were obtained from the National Space Science Data Center, Greenbelt, Maryland.



Accession For		
NTIS GRA&I	<input checked="" type="checkbox"/>	
DTIC TAB	<input type="checkbox"/>	
Unannounced	<input type="checkbox"/>	
Justification		
By _____		
Distribution/		
Availability Codes		
Avail and/or		
Dist	Special	
A		

Contents

1. INTRODUCTION	9
2. RECEIVING SYSTEM AND DATA PROCESSING	12
3. DEFINITION OF STATISTICAL PARAMETERS	13
3.1 RMS Phase Deviation	13
3.2 Phase Spectral Slope and Strength	13
3.3 S_4 Scintillation Index	14
4. RESULTS	14
4.1 Phase Scintillation Statistics	17
4.1.1 RMS Phase Deviation σ_ϕ During the Spring	17
4.1.2 RMS Phase Deviation σ_ϕ During the Summer	19
4.1.3 RMS Phase Deviation σ_ϕ During the Autumn	21
4.1.4 Phase Spectral Intensity T_ϕ	21
4.1.5 Phase Spectral Slope p_ϕ	21
4.2 Intensity Scintillation Statistics	29
4.2.1 Scintillation Index S_4 During the Spring	29
4.2.2 Scintillation Index S_4 During the Summer	29
4.2.3 Scintillation Index S_4 During the Autumn	32
5. COMPARATIVE PHASE SPECTRAL STUDY OF CO-LOCATED WIDEBAND AND FLEETSAT DATA	32
6. CORRELATED MEASUREMENTS OF PARTICLE PRECIPITATION FROM DMSP AND PHASE SCINTILLATIONS	36
7. CONCLUSIONS	51
REFERENCES	57
DISTRIBUTION LIST	61

Illustrations

1a.	Comparison of Subionospheric Track of Typical Overhead Wideband Satellite Pass (observed on 31 March 1979) and 350-km Ionospheric Intersection Point of the Fleetsat Measurements	10
1b.	Position of the Goose Bay Fleetsat Intersection at Magnetic Midnight With Respect to the $Q=7$ Auroral Oval	11
2.	Sample Time Record for 3 February 1979 Showing Interruptions of the CW Mode by FSK Transmissions	15
3a.	Phase Scintillation Index σ_ϕ vs UT During the Spring Under Quiet Magnetic Conditions	17
3b.	Phase Scintillation Index σ_ϕ vs UT During the Spring Under Disturbed Magnetic Conditions	18
4a.	Phase Scintillation Index σ_ϕ vs UT During the Summer Under Quiet Magnetic Conditions	20
4b.	Phase Scintillation Index σ_ϕ vs UT During the Summer Under Disturbed Magnetic Conditions	20
5a.	Phase Scintillation Index σ_ϕ vs UT During the Autumn Under Quiet Magnetic Conditions	22
5b.	Phase Scintillation Index σ_ϕ vs UT During the Autumn Under Disturbed Magnetic Conditions	22
6a.	Spectral Strength T_ϕ of Phase at 1 Hz vs UT During the Spring Under Quiet Magnetic Conditions	23
6b.	Spectral Strength T_ϕ of Phase at 1 Hz vs UT During the Spring Under Disturbed Magnetic Conditions	23
7a.	Spectral Strength T_ϕ of Phase at 1 Hz vs UT During the Summer Under Quiet Magnetic Conditions	24
7b.	Spectral Strength T_ϕ of Phase at 1 Hz vs UT During the Summer Under Disturbed Magnetic Conditions	24
8a.	Spectral Strength T_ϕ of Phase at 1 Hz vs UT During the Autumn Under Quiet Magnetic Conditions	25
8b.	Spectral Strength T_ϕ of Phase at 1 Hz vs UT During the Autumn Under Disturbed Magnetic Conditions	25
9a.	Phase Spectral Index p_ϕ vs UT During the Spring Under Quiet Magnetic Conditions	26
9b.	Phase Spectral Index p_ϕ vs UT During the Spring Under Disturbed Magnetic Conditions	26
10a.	Phase Spectral Index p_ϕ vs UT During the Summer Under Quiet Magnetic Conditions	27
10b.	Phase Spectral Index p_ϕ vs UT During the Summer Under Disturbed Magnetic Conditions	27
11a.	Phase Spectral Index p_ϕ vs UT During the Autumn Under Quiet Magnetic Conditions	28
11b.	Phase Spectral Index p_ϕ vs UT During the Autumn Under Disturbed Magnetic Conditions	28

Illustrations

12a.	Intensity Scintillation Index S_4 vs UT During the Spring Under Quiet Magnetic Conditions	30
12b.	Intensity Scintillation Index S_4 vs UT During the Spring Under Disturbed Magnetic Conditions	30
13a.	Intensity Scintillation Index S_4 vs UT During the Summer Under Quiet Magnetic Conditions	31
13b.	Intensity Scintillation Index S_4 vs UT During the Summer Under Disturbed Magnetic Conditions	31
14a.	Intensity Scintillation Index S_4 vs UT During the Autumn Under Quiet Magnetic Conditions	33
14b.	Intensity Scintillation Index S_4 vs UT During the Autumn Under Disturbed Magnetic Conditions	33
15.	Comparison of Phase Scintillation Index σ_ϕ of Wideband (138 MHz) and Fleetsat (244 MHz) as Seen From Goose Bay, Labrador on 31 March 1979	34
16.	Comparison of Phase Spectral Index p_ϕ of Wideband (138 MHz) and Fleetsat (244 MHz) at the Time of Closest Approach of Wideband to the Fleetsat Intersection as Noted in Figure 15	35
17.	The DMSP/F2 Satellite Track Projected Along the Magnetic Field Line to 110 km for Orbit 9380 From Which Particle Data Were Obtained for the 29 March 1979 Study	37
18a.	The Interplanetary Magnetic Field B_z , Planetary Magnetic Index K_p , and Auroral Electrojet Index AE Data for 29 March 1979	38
18b.	The Horizontal Component of the Goose Bay Magnetogram on 29 March 1979 Showing a 400 γ Negative Bay	39
19.	Energetic Electron Measurement Over the Northern Polar Cap for Orbit 9380 on 29 March 1979 (0140 - 0202 UT)	40
20.	Enlarged View of the Evening Auroral Oval Precipitation Region for Orbit 9380 on 29 March 1979 (0157 - 0202 UT)	41
21a.	Ten Differential Energy Spectra for Ten Successive Seconds of DMSP Precipitating Electron Data Taken From Orbit 9380 on 29 March 1979 Poleward of the Fleetsat Intersection Between 015950 - 015959 UT Showing Smooth Variations in JTOT, JETOT and EAVE and a Quasi-thermal Spectrum	42
21b.	Same as in Figure 21a But Showing Decrease in High Energy Flux and Increase in Lower Energies Between 020010 - 020019 UT	43
21c.	Same as in Figure 21a but Showing Monotonic Increasing Fluxes With Decreasing Energy Down to 47 eV Between 020030 - 020039 UT	44
22.	Differential Flux Measurements of the 47, 73, 112 eV and 5.5 keV Energy Channels From Orbit 9380 Showing the Change in Particle Spectrum With Latitude	45

Illustrations

23.	Total Electron Content (TEC) Measurements From the ATS-5 Satellite Measured at Goose Bay, Labrador on 29 March 1979 Showing Onset of TEC Increase at Approximately 0150 UT	46
24.	Time Record of Phase and Amplitude Fluctuations of Fleetsat From Goose Bay on 29 March 1979 Detrended With a Filter Cutoff of 0.0067 Hz	47
25.	Intensity and Phase Scintillation Parameters S_4 , σ_ϕ , T_ϕ and p_ϕ of Goose Bay FLEETSAT on 29 March 1979 (01-04 UT)	49
26a.	Sample Power Spectrum of Phase Scintillation on 29 March 1979, 015850-020538 UT at a Time When $\sigma_\phi = 14.3$ Rad	50
26b.	Sample Power Spectrum of Phase Scintillation on 29 March 1979, 020538-021218 UT at a Time When $\sigma_\phi = 12.08$ Rad	50
27a.	Sample Power Spectra of Amplitude Scintillations on 29 March 1979 Between 015850 and 020538 UT with $S_4 = 0.60$ and Between 013218 and 013858 UT With $S_4 = 0.18$ Showing Similar Values of the Fresnel Frequency	52
27b.	Same as in Figure 27a but for 29 March 1979 Between 020538 and 021218 UT With $S_4 = 0.46$ and 31 March 1979 Between 045419 and 050059 UT With $S_4 = 0.51$ Showing Very Different Values of the Fresnel Frequency	52
28.	Ion Density Measurements From the DMSP/F2 Thermal Plasma Monitor for Orbit 9380 on 29 March 1979 at a Time Coordinated With the Particle Precipitation Data of Figure 20	54

Tables

1.	Comparison of Phase Spectral Indices, Goose Bay, 31 March 1979	36
----	--	----

Phase and Amplitude Scintillation Statistics at 244 MHz From Goose Bay Using a Geostationary Satellite

1. INTRODUCTION

A recent report,¹ hereafter referred to as Report 1, has documented the scintillation statistics observed from two longitude sectors of the auroral oval. The primary focus of the report was the study of phase scintillations at 138 MHz using the coherent transmissions emitted by the orbiting Wideband satellite. The satellite orbit, however, was sun-synchronous and thus observations were only available near local midnight and during pre-noon hours. To extend the coverage over a 24-hour period, a novel system of measuring phase scintillations using transmissions from a geostationary satellite was put into operation at Goose Bay. To our knowledge, this is the first time that an extended set of ground observations has been made to measure phase scintillations on a continuous basis using this technique. A limited number of airborne observations have been made by the Air Force Wright Aeronautical Laboratories using a similar technique.²

(Received for publication 6 August 1982)

1. Basu, Sunanda, Basu, S., Livingston, R. C., Whitney, H. E., and MacKenzie, E. (1981) Comparison of Ionospheric Scintillation Statistics From the North Atlantic and Alaskan Sectors of the Auroral Oval Using the Wideband Satellite, AFGL-TR-81-0266, ADA111871.
2. Prettie, C. W. (1981) Phase Effects of Ionospheric Irregularities, AFWAL-TR-81-1163.

This report presents the phase and amplitude scintillation statistics observed from Goose Bay, Labrador using the observation system mentioned above which utilized the 244-MHz transmissions from the geostationary satellite Fleetsat located near the equator at 100°W longitude. The period of observations was from January to November, 1979 and thus overlapped the period of Wideband observations discussed in Report 1. The 350-km ionospheric intersection point for the Fleetsat measurements is 47.9°N, 67.9°W as shown in Figure 1a. The sub-ionospheric track of a typical overhead Wideband satellite pass observed on 31 March 1979, which passed very close to the Fleetsat observation point is shown for comparison. In Section 5 of the report we shall compare the phase scintillation spectra obtained utilizing transmissions of the orbiting and the geostationary satellites when the two observation volumes were co-located.

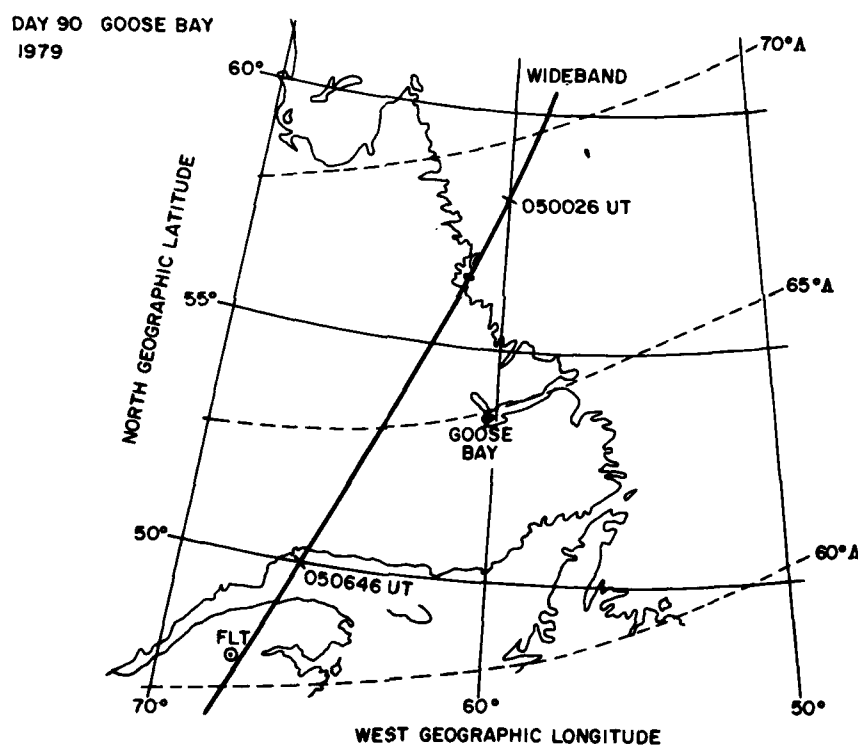


Figure 1a. Comparison of Subionospheric Track of Typical Overhead Wideband Satellite Pass (observed on 31 March 1979) and 350-km Ionospheric Intersection Point of the Fleetsat Measurements

The invariant latitude of the Fleetsat intersection is 60° so that in general, under magnetically quiet conditions, the auroral oval is poleward of this point. A detailed discussion of such considerations has been provided by Basu and Aarons³ in their auroral amplitude scintillation morphology paper. Figure 1b shows the position of the Fleetsat intersection point from Goose Bay with respect to the $Q = 7$ auroral oval.⁴ The auroral oval representation is reproduced from Whalen.⁵ The observation point will thus be able to monitor auroral irregularities only during large magnetic storms. The scintillation and particle precipitation characteristics observed for one such large storm will be presented in Section 6. In general, however, the scintillation characteristics at the observation point are expected to be those that pertain to the ionospheric trough region which are rather quiet (McClure and Hanson,⁶ Basu,⁷ Basu and Aarons³).

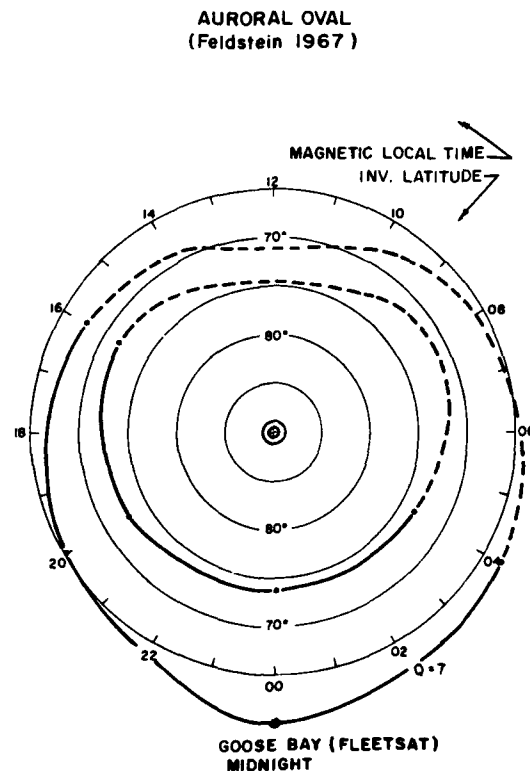


Figure 1b. Position of the Goose Bay Fleetsat Intersection at Magnetic Midnight With Respect to the $Q = 7$ Auroral Oval

(Due to the large number of references cited above, they will not be listed here. See References, page 57.)

2. RECEIVING SYSTEM AND DATA PROCESSING

The measurements described in the following sections were made using an extended dynamic range receiver with an extremely stable local oscillator. The receiver operates under computer control and once tuned to within a few hertz of a signal detected in a 10-Hz bandwidth, self-tunes to within ± 1 millihertz of the mean frequency as determined by the zero crossings averaged over a 20-sec period. Subsequent changes in frequency, either due to changes in ionospheric or geometrical doppler, are sensed by the system, which then retunes. At each retune, the local oscillator frequency information is recorded to allow reconstruction of the long-term phase in subsequent processing. In this way the system can measure signal phase variations with precision as would a coherent system except for any long-term relative frequency drifts between the satellite and receiver references.

Once a signal is properly acquired by the receiver, its quadrature components are sampled at 10 Hz and are digitally recorded along with time and pertinent system information. During initial off-line processing, these data are converted to signal intensity and continuous phase. While simple in concept, the generation of continuous phase over long observation periods is prone to numerical difficulties. Since this is a single frequency measurement, the accumulation of phase over a period of several hours can result in extremely large values. These problems have been avoided by calculation and removal of the largest scale (for example, few hours) dispersive doppler changes during pre-processing.

Following initial processing, only phase variations with periods shorter than some tens of minutes remain. The data can then be treated using methods similar to those designed for, and proven, during the Wideband and Microwideband experiments (Fremouw et al⁸; Basu et al¹). Basically, this consists of separation of rapidly varying scintillation components of the signal from the longer term trends. The spectral components are separated by passing the phase data through a sharp cutoff high pass digital filter ($f_c = 0.0067$ Hz); there is generally no need to filter signal intensity, which has no low frequency component in the constant signal level, geostationary case. The most significant difference between the geostationary satellite and the orbiting Wideband satellite is that the space-to-time conversion which dictates the distribution of energy in the phase spectrum is now dictated by irregularity drift, and not satellite motion. The detrend cutoff frequency is, accordingly, much lower. A further discussion of this point is presented in Section 4.

8. Fremouw, E.J., Leadabrand, R.L., Livingston, R.C., Cousins, M.D., Rino, C.L., Fair, B.C., and Long, R.A. (1978) Early results from the DNA Wideband satellite experiment - complex-signal scintillation, Radio Sci. 13:167.

3. DEFINITION OF STATISTICAL PARAMETERS

Following phase detrending, the signal variations are statistically characterized by calculation of the parameters listed below. These are analogous to those defined in Report 1 but obviously the detrending periods and sample sizes are different to reflect the very different orbital characteristics of the satellites in the two cases.⁹

3.1 RMS Phase Deviation

The standard deviation of the detrended phase component is calculated as

$$\sigma_{\phi} = (\langle \phi^2 \rangle - \langle \phi \rangle^2)^{1/2} \quad (1)$$

in radians as measured at the receiver output. Note that this parameter is dependent upon the detrend cutoff frequency. For the routine analysis a detrending frequency of 0.0067 Hz was used as mentioned in Section 2.

3.2 Phase Spectral Slope and Strength

We assume a power-law form of the phase power spectral density, $\Phi_{\phi}(f)$, as has been displayed by Wideband and ATS-6 data, in the form

$$\Phi_{\phi}(f) = T_{\phi} f^{p_{\phi}} \quad (2)$$

where p_{ϕ} is the slope, and T_{ϕ} is the strength in mks units.⁸ These parameters are extracted from a linear least-squares fit to the log-log phase spectrum over the range of 0.025 to 0.5 Hz. The T_{ϕ} values to be presented in the next section are the extrapolated spectral strengths obtained at 1 Hz.

The advantage of using T_{ϕ} and p_{ϕ} is that unlike σ_{ϕ} , they characterize the phase disturbance independent of the detrend cutoff. Generally the T_{ϕ} and p_{ϕ} are consistent with σ_{ϕ} , although σ_{ϕ} can include energy outside of the slope-fit range. It is recommended, therefore, that σ_{ϕ} , T_{ϕ} , and p_{ϕ} all be considered together. Some examples of phase spectra will be shown in conjunction with special event studies in Sections 5 and 6.

9. Livingston, R.C. (1980) Micro-Wideband Analysis Summary Output—Geosynchronous and Near-Synchronous Beacons, Technical Memorandum, SRI International, Menlo Park, California.

3.3 S_4 Scintillation Index

Normalized standard deviation of intensity

$$S_4 = [(\langle I^2 \rangle - \langle I \rangle^2) / \langle I \rangle^2]^{1/2} \quad (3)$$

ranges from 0 to about 1.2 from quiet to strong scatter conditions. The S_4 index was first introduced by Briggs and Parkin.¹⁰

The intensity spectral strength T_1 and slope p_1 that were discussed in Report 1 are not presented for this data set. This is because the median S_4 level is in general so low that the spectral intensity at 1 Hz merely samples the noise level and p_1 pertains to such noise-like spectra. However, some examples of intensity spectra will be shown in conjunction with special event studies in Section 6.

4. RESULTS

As a supplement to the previously mentioned Wideband study presented in Report 1, phase and amplitude scintillation observations of the geostationary satellite Fleetsat have been conducted at Goose Bay, Labrador for a 10-month period in 1979. The elevation angle of the observations is 20° and the azimuth is -135° . Thus, observations are made at a relatively low angle and irregularity anisotropy effects, such as the geometrical enhancement for both rod-like and sheet-like irregularities so prominent in the Wideband data, cannot be observed. Although the observations pertain to a single intersection point, and this point is such that it is expected to show considerable activity only during large magnetic disturbances, the continuous measurements with geostationary satellites over a 10-month data collection period does allow a full diurnal coverage and a 3-season comparison to supplement the Goose Bay Wideband seasonal plots. To conform with Report 1, the data have been separated into three periods to study the seasonal behavior: (1) Feb through Apr data that are approximately centered on the vernal equinox and labeled Spring; (2) May through July data that are approximately centered on the June solstice and labeled Summer; and (3) Aug through Oct data that are approximately centered on the autumnal equinox and labeled Autumn.

The phase and amplitude scintillation statistics were computed over consecutive 400-sec intervals in the course of the 24-hour period of operation. While in principle continuous operation was possible, the transmission schedule was such that only 2 to 3 days per week were recorded and there were quite a few data gaps caused by receiver and transmission problems. In particular, during the January-

10. Briggs, B. H., and Parkin, I. A. (1963) On the variation of radio star and satellite scintillations with zenith angle, J. Atmos. Terr. Phys. 25:339.

April, 1979 period the data were vitiated by momentary breaks from the CW to an FSK mode of transmission. The time record for a span of detrended data with this problem is shown in Figure 2. Obviously both the phase and amplitude scintillation indices are elevated by the bursts of modulation, despite the lack of significant ionospheric structure. For instance, between 06 and 10 UT when there is no significant ionospheric structure, σ_ϕ is ~ 0.1 rad and S_4 is ~ 0.07 which is close to the noise threshold of the system. However, during the worst phase of FSK contamination between 1200 and 1300 UT, σ_ϕ varies between 1.0 and 5.0 rad and S_4 varies between 0.1 and 0.2. Thus the σ_ϕ values are seriously affected by this problem. Various tests were devised for computer recognition of such problems in routine data analysis but it was not found possible to identify all of such FSK contaminated data. Beginning in May, 1979, however, CW transmissions were requested for specific dates and during such times the FSK problem was minimized.

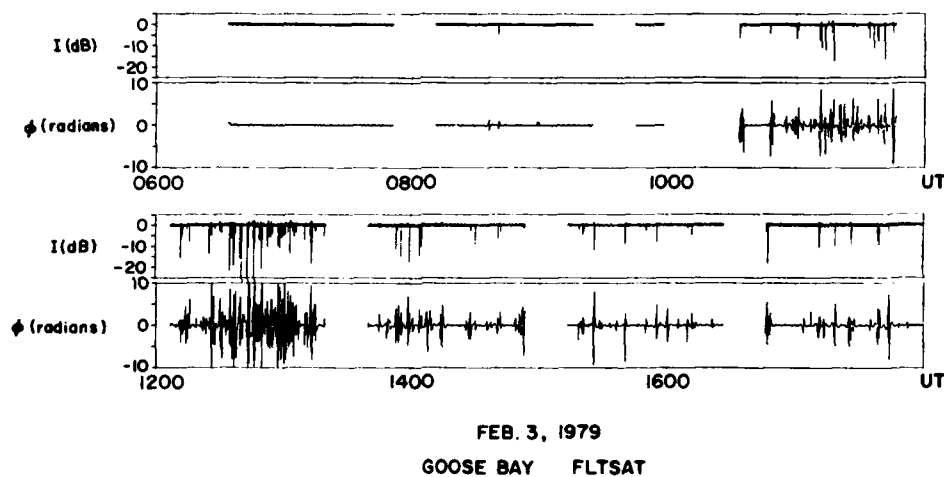


Figure 2. Sample Time Record for 3 Feb 1979 Showing Interruptions of the CW Mode by FSK Transmissions. In a time period with no significant ionospheric structure (1200-1300 UT) the FSK contamination results in σ_ϕ varying between 1 and 5 rad

The temporal variation of the scintillation parameters is presented in a large number of graphs as in Report 1 for the benefit of the user. The 400-sec values of σ_ϕ , T_ϕ , p_ϕ , and S_4 are sorted into 2-hr UT bins for $K_p < 3.5$ (quiet magnetic conditions) and $K_p > 3.5$ (magnetically disturbed conditions) to maintain parity with Report 1 even though it is realized that larger magnetic disturbances may be necessary to produce substantial scintillation effects at the Fleetsat intersection point. The 50th and 90th percentile occurrence statistics are computed and plotted for these 2-hr UT blocks. The lowest and highest number of 400-sec data samples per 2-hr

UT block are specified on the graphs to give an idea of the size of the data base. At some time intervals, there may be no data or insufficient data to establish the 90th percentile level. At these times, the lines are shown as dashed. We propose to present the phase scintillation statistics observed during the three seasons first. These are followed by the intensity statistics observed during the same seasons. Since only a small amount of data are available for the months of January and November, in the statistics the few days in January are included with the spring (Feb-Apr) data while the few November days are included with the autumn (Aug-Oct) data.

To compare the following results with those given in Report 1, the user should be aware of several factors. The most obvious factor is the difference in the frequency between the two data sets: Wideband statistics were computed at 138 MHz(f_1) while Fleetsat statistics were computed using transmissions obtained at 244 MHz(f_2). Based on the weak scatter theory and on the assumption of a value of 4 for the 3-dimensional spectral index of the irregularities, the Wideband amplitude scintillation results have to be reduced by the factor $(f_2/f_1)^{1.5}$ (Rufenach,¹¹ Rino¹²) that is, a factor of 2.4 for Wideband amplitude statistics observed in the Goose Bay sector at $\sim 60^\circ\Lambda$. For phase statistics the scattering regime does not necessarily have to be weak; the scaling law will require the Wideband phase scintillation index to be reduced by f_2/f_1 , that is, a factor of 1.8 (Fremouw et al).⁸ However, one must also consider the fact that a detrending interval of 10 sec ($f_c = 0.1$ Hz) for Wideband phase is equivalent to a detrending interval of 150 sec ($f_c = 0.0067$ Hz) for Fleetsat if the effective ionospheric E-W drift, that is, the component of drift perpendicular to the Fleetsat propagation path, is 200 m/sec. This is because the ray path of the Wideband satellite travels through the high latitude F-region across magnetic field lines at a velocity of approximately 3 km/sec, which is a factor of 15 greater than the assumed effective ionospheric drift. It should be noted that because the azimuth of the Fleetsat measurements is -135° , the effective E-W drift will be a factor of 1.4 smaller than the actual drifts. Obviously in the Fleetsat case, the geometry is unique and because of the low elevation measurements, it is not so much the effect of the anisotropy as the increased path length that controls the scintillation magnitude. Moreover, since Goose Bay was the observing station for both the Wideband and Fleetsat data sets, these factors affect both data sets in a similar fashion if only the $60^\circ\Lambda$ Wideband data is used for comparison.

11. Rufenach, C. L. (1975) Ionospheric scintillation by a random phase screen: spectral approach, Radio Sci. 10:155.
12. Rino, C. L. (1979) A power law phase screen model for ionospheric scintillation. 1. Weak scatter, Radio Sci. 14:1135.

4.1 Phase Scintillation Statistics

4.1.1 RMS PHASE DEVIATION σ_ϕ DURING THE SPRING

The phase scintillation σ_ϕ in radians as a function of UT for magnetically quiet ($K_p < 3.5$) Fleetsat data for Jan-Apr 1979 is shown in Figure 3a, with the corresponding magnetically disturbed ($K_p > 3.5$) data shown in Figure 3b. The corrected geomagnetic midnight (CM) and noon (CN) are indicated. Figure 3a shows a median level of σ_ϕ less than 1 rad for the nighttime hours. The second pre-noon peak of σ_ϕ which does not have a counterpart in S_4 (as shown later in Figure 12a) is, unfortunately, due to FSK contamination referred to earlier. In Figure 2 we have shown an example of the time record on 3 Feb 1979 when FSK was particularly severe from 1000 to 1400 UT. The two other seasons for which CW transmissions were requested do not show this peak. The 90th percentile shows a strong nighttime peak of 3-4 rad during nighttime hours and a second daytime peak obviously caused by FSK. It should be noted that the spring nighttime phase scintillations are larger than those observed in the other seasons (see Figures 4a and 5a). Since the corresponding S_4 behavior is consistent with the above statement, it is hoped that FSK contamination is not appreciable for the nighttime data. Further, this follows the pattern found earlier by Basu and Aarons.³

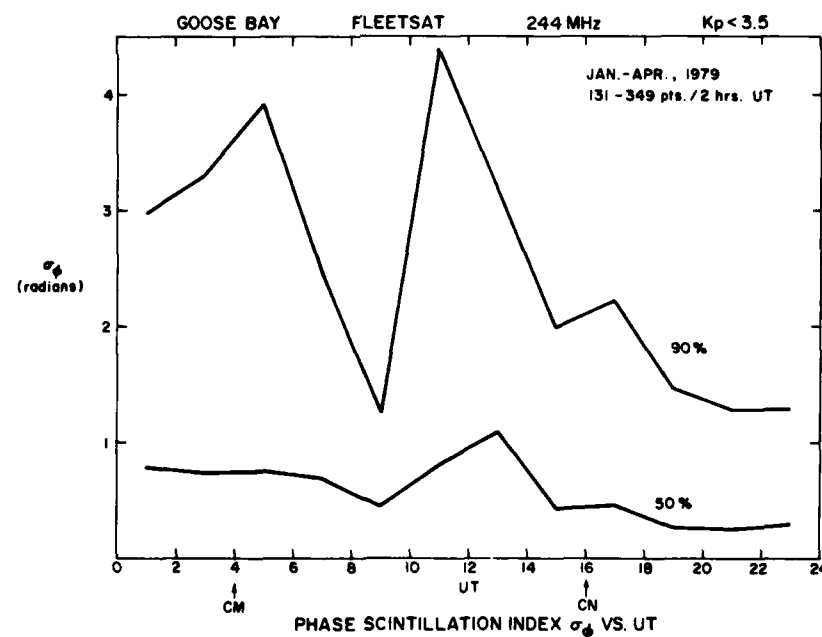


Figure 3a. Phase Scintillation Index σ_ϕ vs UT During the Spring Under Quiet Magnetic Conditions. Corrected geomagnetic midnight (CM) and noon (CN) are marked

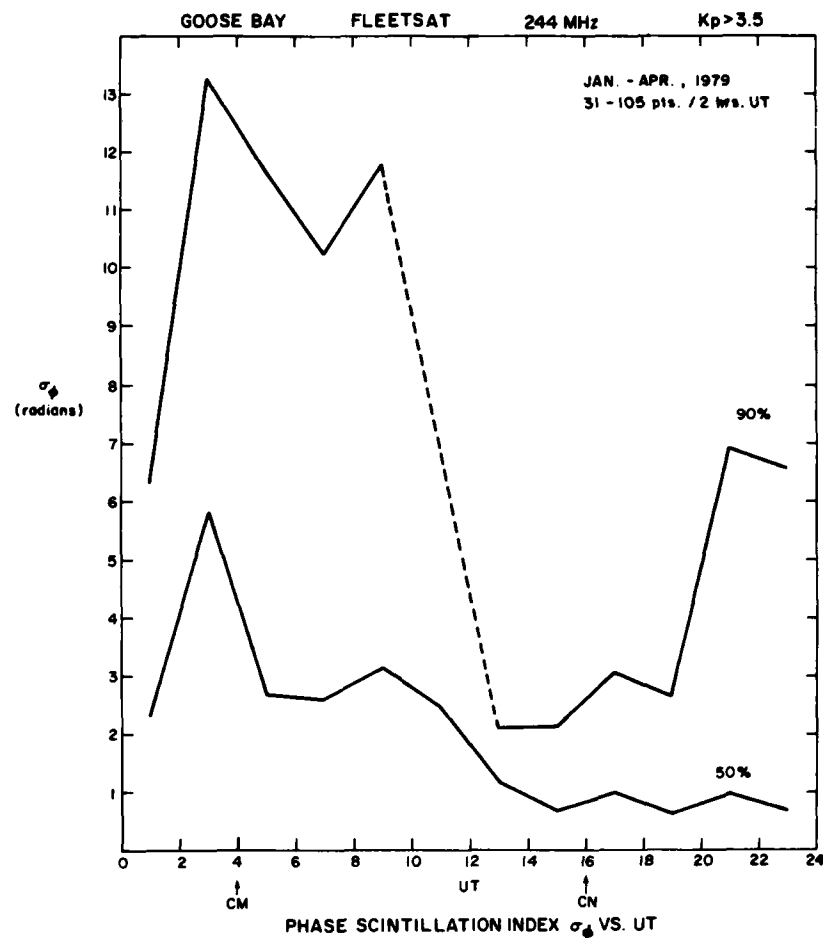


Figure 3b. Phase Scintillation Index σ_ϕ vs UT During the Spring Under Disturbed Magnetic Conditions

The magnetically disturbed data for Jan-Apr (Figure 3b) shows a strong night-time peak in the median of 6 rad in the time interval 02-04 UT, with post-local-midnight values of 2-3 rad. The 90th percentile curve shows a 13 rad peak, also in the time period 02-04 UT. This large increase in σ_ϕ from quiet to disturbed magnetic conditions (6-fold in the 50th percentile, 3-fold in the 90th percentile) is not seen nearly as dramatically in the other seasons. The double hump seen in the night-time magnetically disturbed phase data in all seasons seems to be caused by the equatorward expansion and poleward retraction of the auroral oval past the Fleetsat observation point as was also discussed by Houminer et al.¹³

13. Houminer, Z., Aarons, J., and Rich, F. (1981) Production and dynamics of high-latitude irregularities during magnetic storms, J. Geophys. Res. 86:9939.

In comparison with the Wideband statistics for Jan-Apr, 1979, taking the nighttime median σ_ϕ obtained at $60^\circ\Lambda$ for the two magnetic cases, we find the magnetically disturbed σ_ϕ (~ 2 rad, see Figure 80, Report 1) about twice the magnetically quiet σ_ϕ (~ 1 rad, see Figure 78, Report 1). The daytime Fleetsat σ_ϕ values are about 3 times the expected scaled values from Wideband. However, since we are dealing with σ_ϕ numbers close to the noise threshold of the systems, it is difficult to come to definite conclusions. While scaling by a factor of 1.7 provides a reasonable agreement with the quiet Fleetsat σ_ϕ shown in Figure 3a, the value shown in Figure 3b is 5 times the scaled value expected from Wideband measurements. This is a very interesting result and is in all probability due to the much larger drift velocities that are generally observed in the trough (Smiddy et al¹⁴) and in the auroral region (Wand and Evans¹⁵) during large magnetic storms. It was pointed out earlier that a detrend interval of 10 sec used for Wideband is equivalent to a 150 sec detrend interval on Fleetsat only on the basis of approximately 200 m/sec effective E-W drifts. It is not uncommon according to the references cited above to measure drifts of 500 m/sec to 1 km/sec during large magnetic storms. The fact that S_4 values scale according to expectations (to be discussed in Section 4.2) gives us greater confidence in our hypothesis that the enhancement of drift speeds also contributes to the σ_ϕ increase in addition to an increase in the strength of turbulence C_s (Rino¹²) as a result of magnetic activity.

4.1.2 RMS PHASE DEVIATION σ_ϕ DURING THE SUMMER

Figures 4a and 4b illustrate the Fleetsat phase scintillation data σ_ϕ (radians) observed in May-July 1979 for the magnetically quiet ($K_p < 3.5$) and disturbed ($K_p > 3.5$) cases respectively. Under quiet magnetic conditions (Figure 4a), both the median and the 90th percentile curves are very low, being less than 1 rad. Under disturbed magnetic conditions, the median exhibits a peak of 3 rad in the time interval 02-04 UT. There is usually insufficient data to construct a 90th percentile curve. Compared to the very low median level of σ_ϕ during $K_p < 3.5$, the value of 3 rad during disturbed magnetic conditions appears to be a very significant increase and again is probably related to enhanced drift speeds during magnetic storm conditions. The size of the data base is unfortunately rather small.

14. Smiddy, M., Kelley, M. C., Burke, W., Rich, F., Sagalyn, R., Shuman, B., Hays, R., and Lai, S. (1977) Intense poleward-directed electric fields near the ionospheric projection of the plasmapause, Geophys. Res. Lett. 4:543.

15. Wand, R. H., and Evans, J. V. (1981) The penetration of convection electric fields to the latitudes of Millstone Hill ($\Lambda = 56^\circ$), J. Geophys. Res. 86:5809.

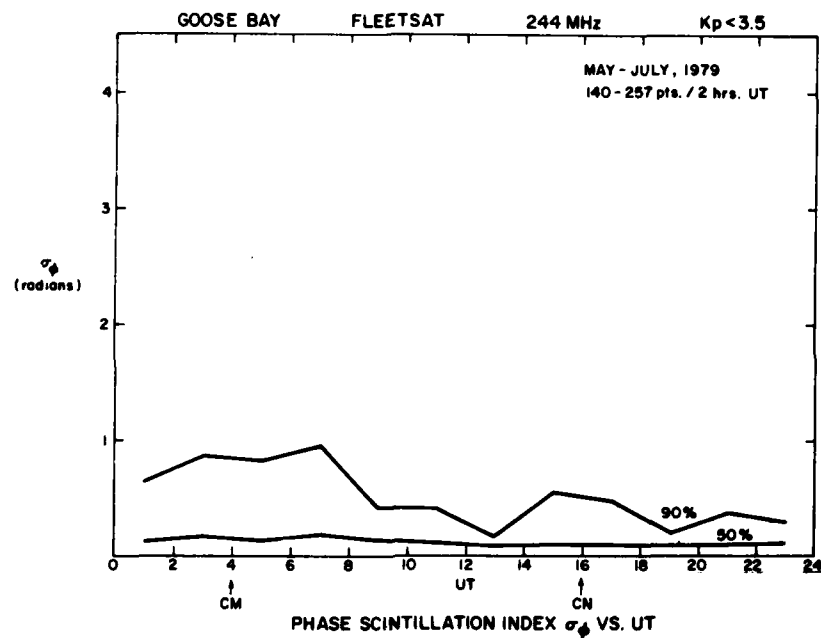


Figure 4a. Phase Scintillation Index σ_ϕ vs UT During the Summer Under Quiet Magnetic Conditions

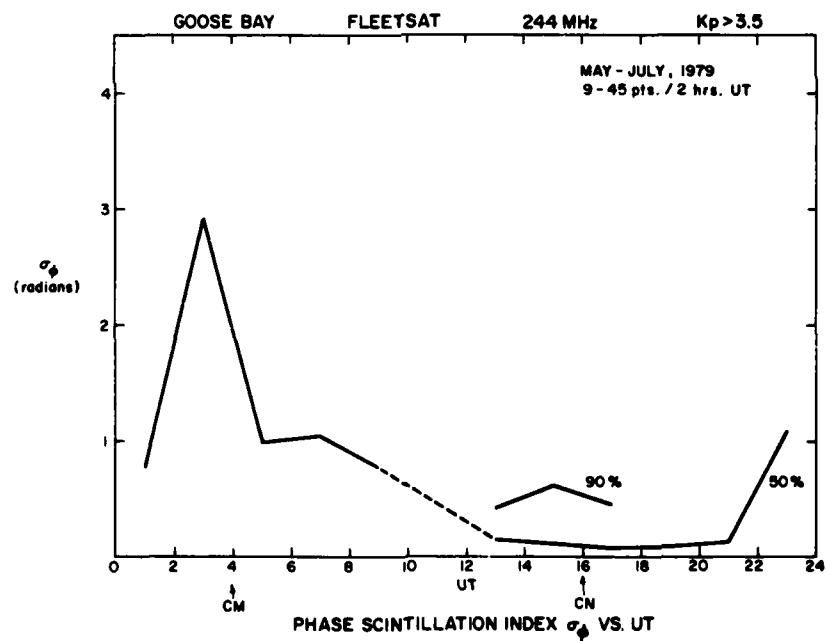


Figure 4b. Phase Scintillation Index σ_ϕ vs UT During the Summer Under Disturbed Magnetic Conditions

A comparison of the Summer Fleetsat phase statistics with the spring phase statistics shows an overall reduction in the summer. The absence of the second peak in the daytime and the very low value of the residuals are obviously made possible by the much lower occurrence of FSK in this season. The reduction of the summer phase values are consistent with Wideband findings presented in Report 1 as well as the earlier amplitude scintillation behavior studied by Basu and Aarons.³

4.1.3 RMS PHASE DEVIATION σ_ϕ DURING THE AUTUMN

Figures 5a and 5b show the magnetically quiet and disturbed cases respectively for the Fleetsat phase data σ_ϕ (radians) taken during Aug-Nov 1979. For $K_p < 3.5$ (Figure 5a) the median curve is very low while the 90th percentile curve is just slightly higher, peaking at about 1.3 rad between 06 and 08 UT. For $K_p > 3.5$ (Figure 5b) the median shows a peak of ~ 2.5 rad at 02-06 UT while the 90th percentile value jumps to ~ 8 rad between 04 and 06 UT. The σ_ϕ behavior in the autumn is similar to that in the summer under both quiet and disturbed conditions (note the different σ_ϕ scales in Figures 4b and 5b).

4.1.4 PHASE SPECTRAL INTENSITY T_ϕ

It was noted in Report 1 and in Section 3 of this report that σ_ϕ depends on the detrend interval used for filtering the raw data while T_ϕ , the phase spectral intensity at 1 Hz, is independent of it. Figures 6-8 give the T_ϕ values derived from Fleetsat observations during magnetically quiet and disturbed conditions in each seasonal group namely, Jan-Apr 1979 (Figures 6a and 6b), May-July 1979 (Figures 7a and 7b), and Aug-Nov 1979 (Figures 8a and 8b). These T_ϕ values at 1 Hz are free of filtering effects and can be used in conjunction with spectral slope (p_ϕ) values to estimate σ_ϕ according to the specific system integration requirements. It is unfortunate, however, that the T_ϕ values seem more susceptible than σ_ϕ to contamination by FSK bursts. Such effects are very evident in both the median and 90th percentile curves in the vernal equinox period (Figure 6a) and the 90th percentile curve during the summer (Figure 7a).

4.1.5 PHASE SPECTRAL SLOPE p_ϕ

The median p_ϕ curves (Figures 9-11) uniformly show a value greater than 2 with the most likely value ranging between 2.2 and 2.5 with p_ϕ closer to 2.7 under disturbed magnetic conditions when σ_ϕ values are higher. A value of 3 would be expected from a one-dimensional in-situ spectral index of 2. It is important to note that these p_ϕ values are consistently higher than those shown in the Wideband statistics presented in Report 1. This statement also holds for the coordinated volume study of phase spectra obtained from Wideband and Fleetsat for 31 March 1979 that will be presented in Section 5.

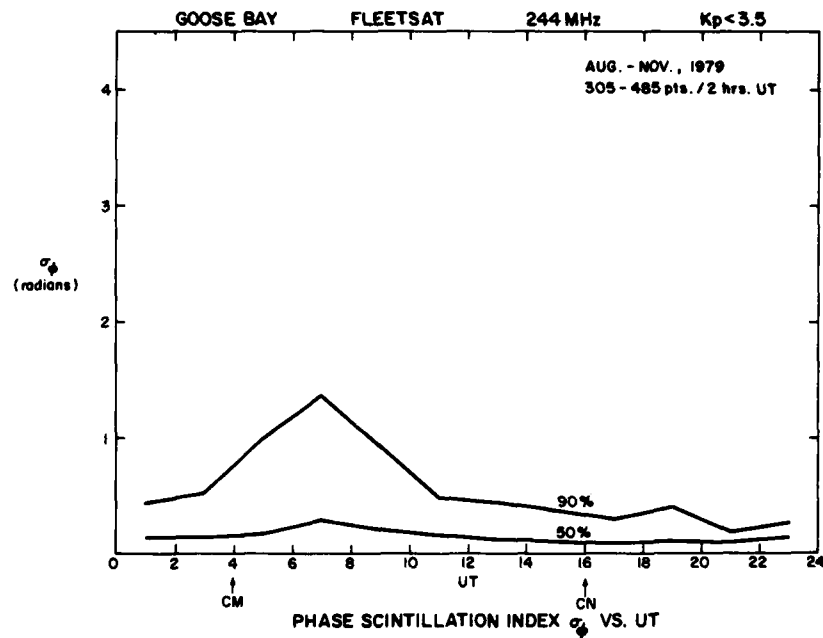


Figure 5a. Phase Scintillation Index σ_ϕ vs UT During the Autumn Under Quiet Magnetic Conditions

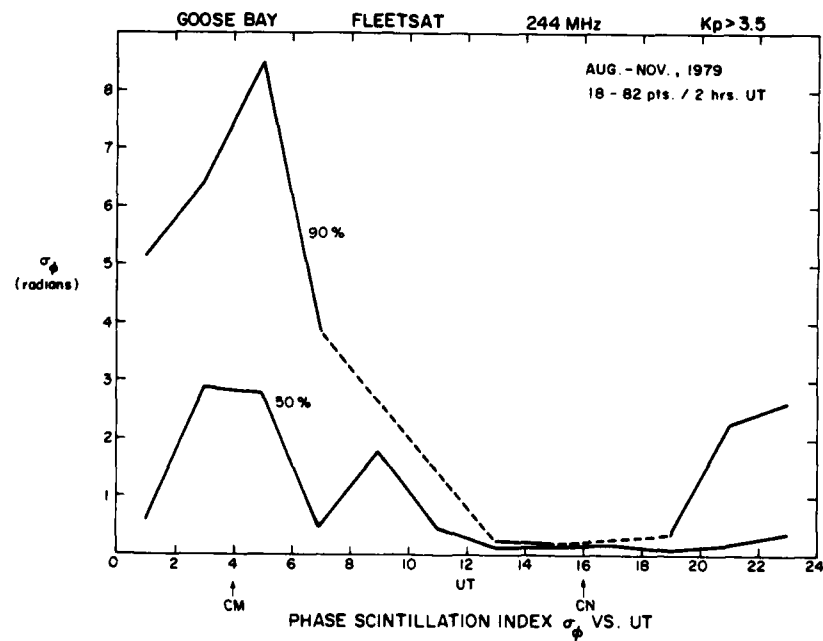


Figure 5b. Phase Scintillation Index σ_ϕ vs UT During the Autumn Under Disturbed Magnetic Conditions

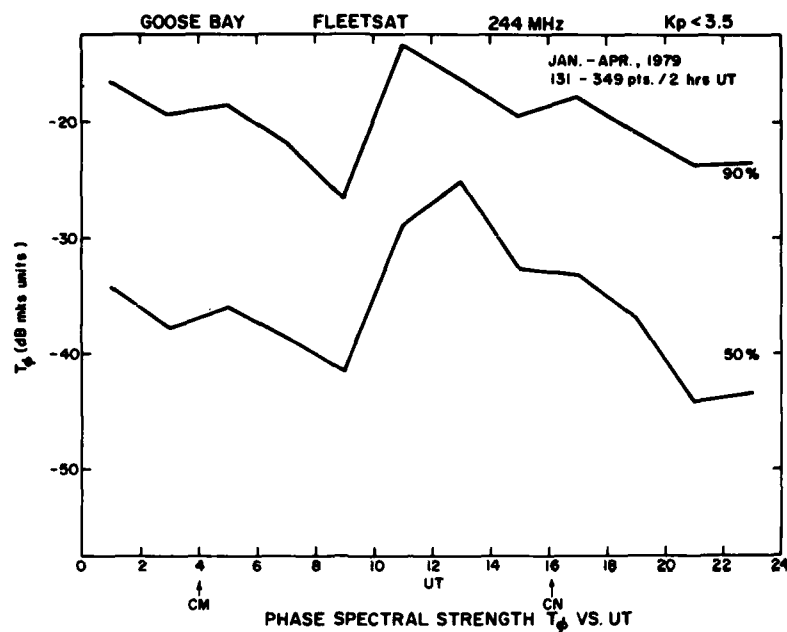


Figure 6a. Spectral Strength T_ϕ of Phase at 1 Hz vs UT During the Spring Under Quiet Magnetic Conditions

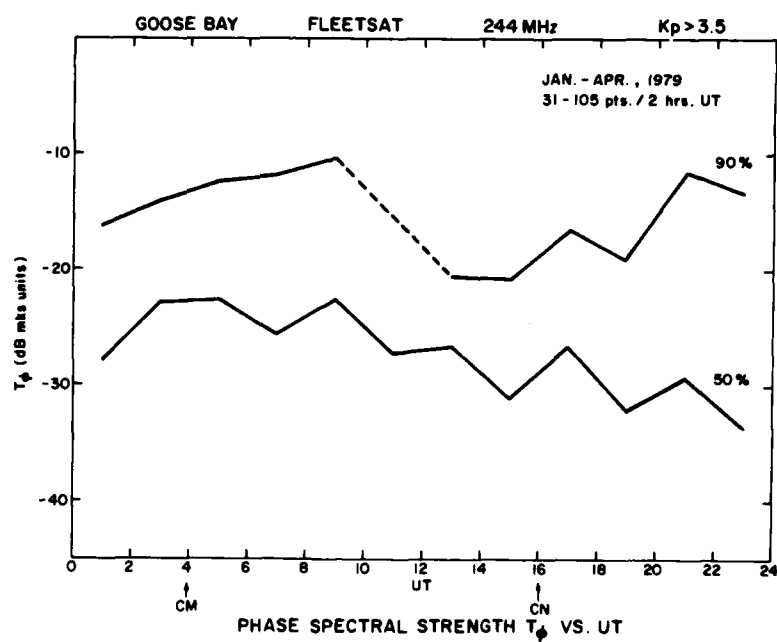


Figure 6b. Spectral Strength T_ϕ of Phase at 1 Hz vs UT During the Spring Under Disturbed Magnetic Conditions

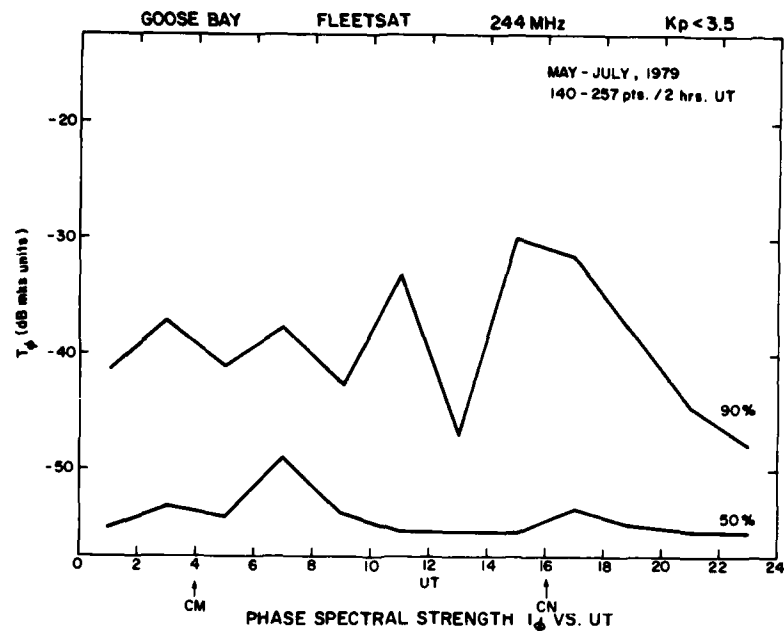


Figure 7a. Spectral Strength T_ϕ of Phase at 1 Hz vs UT During the Summer Under Quiet Magnetic Conditions

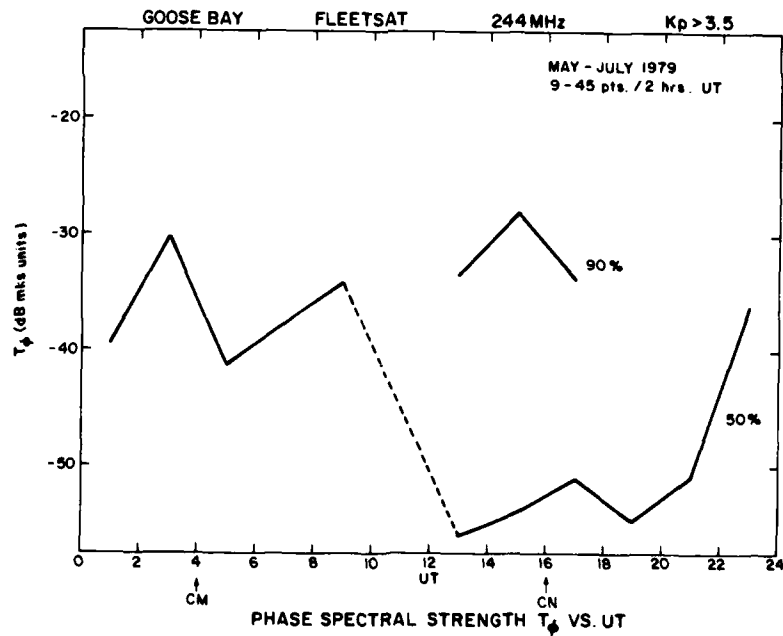


Figure 7b. Spectral Strength T_ϕ of Phase at 1 Hz vs UT During the Summer Under Disturbed Magnetic Conditions

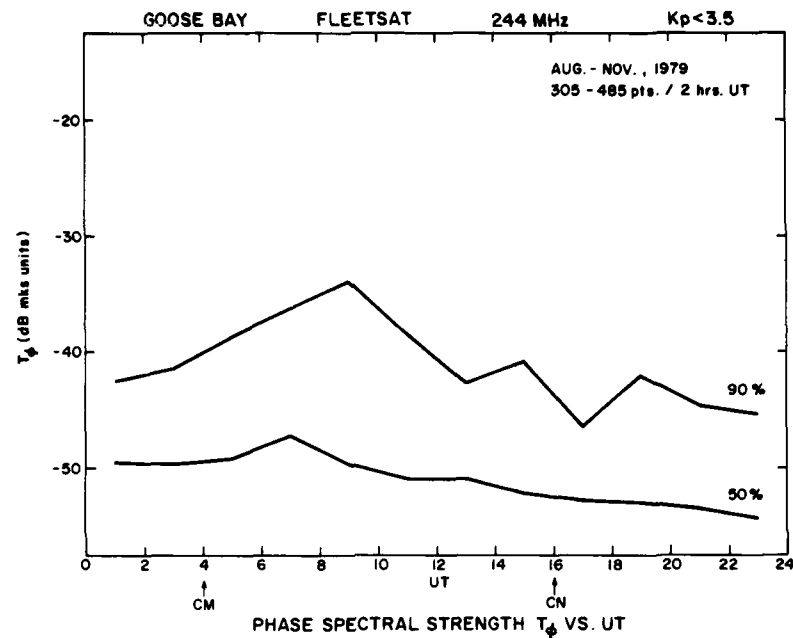


Figure 8a. Spectral Strength T_ϕ of Phase at 1 Hz vs UT During the Autumn Under Quiet Magnetic Conditions

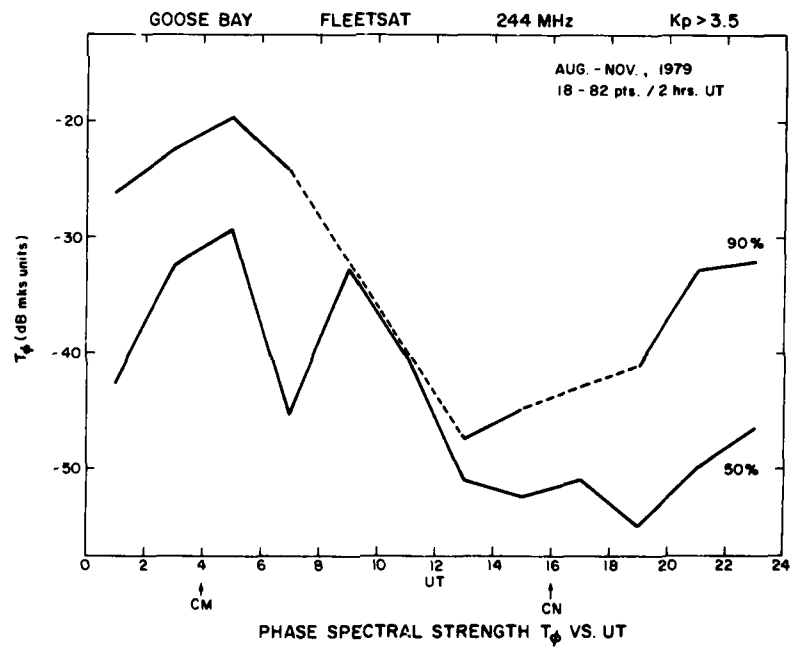


Figure 8b. Spectral Strength T_ϕ of Phase at 1 Hz vs UT During the Autumn Under Disturbed Magnetic Conditions

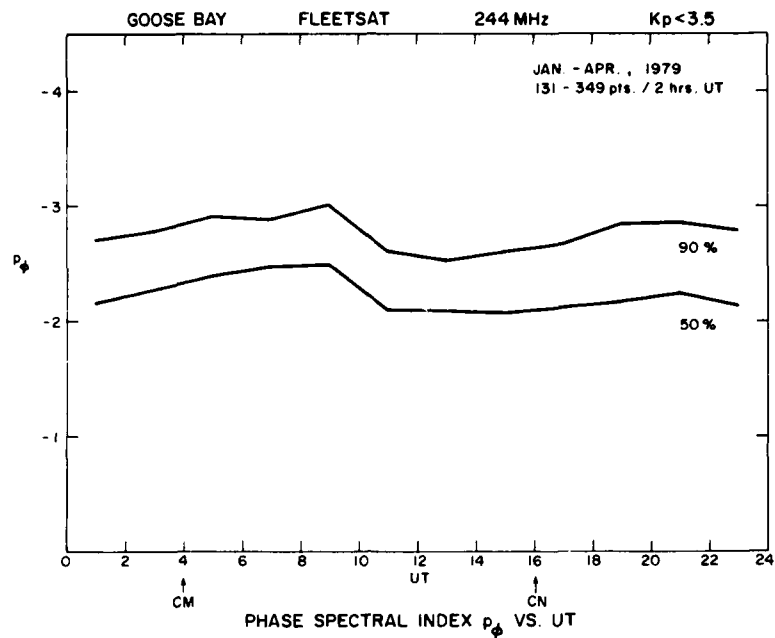


Figure 9a. Phase Spectral Index p_ϕ vs UT During the Spring Under Quiet Magnetic Conditions

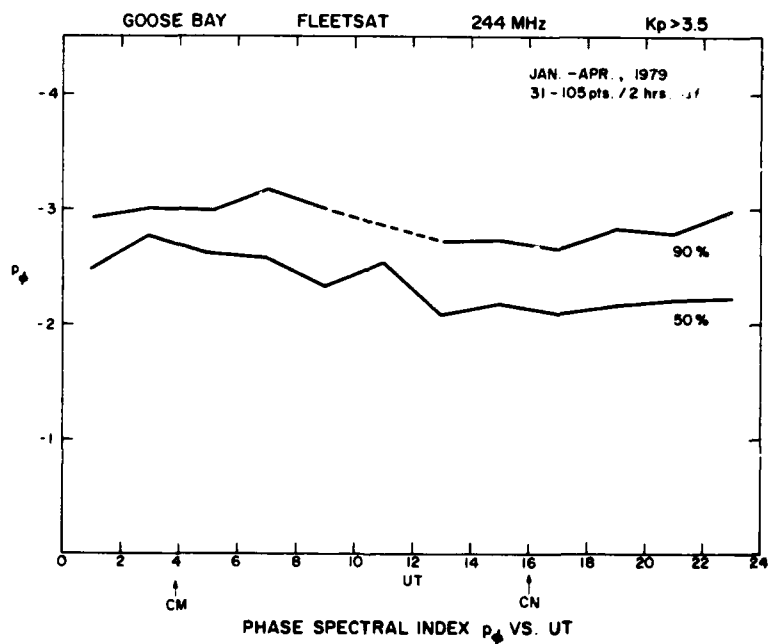


Figure 9b. Phase Spectral Index p_ϕ vs UT During the Spring Under Disturbed Magnetic Conditions

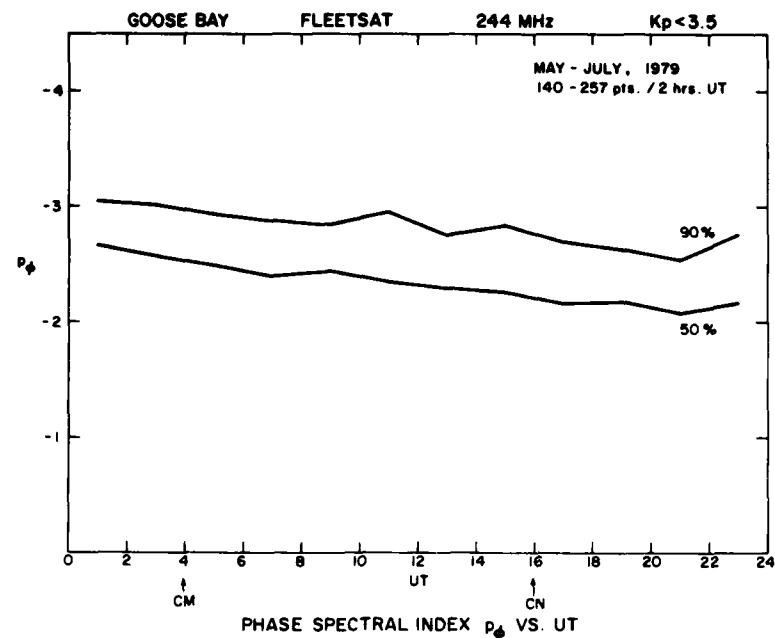


Figure 10a. Phase Spectral Index p_ϕ vs UT During the Summer Under Quiet Magnetic Conditions

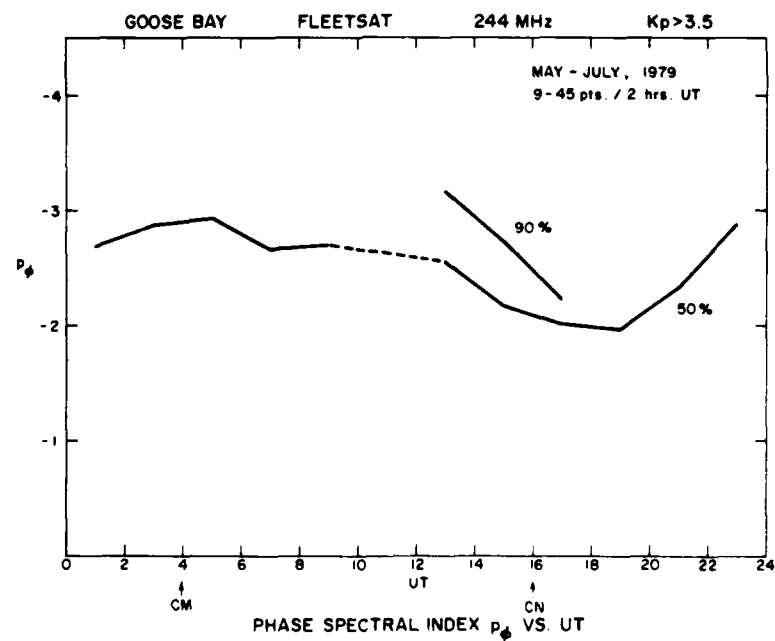


Figure 10b. Phase Spectral Index p_ϕ vs UT During the Summer Under Disturbed Magnetic Conditions

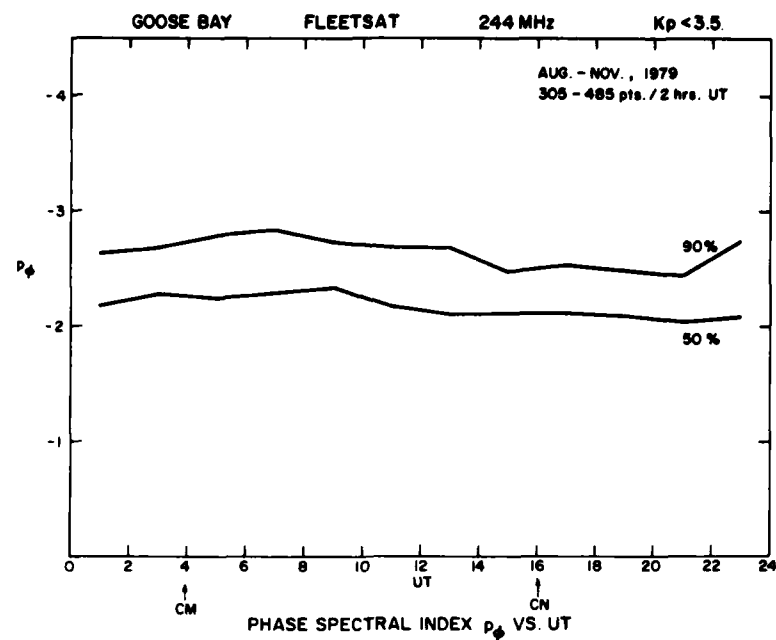


Figure 11a. Phase Spectral Index p_ϕ vs UT During the Autumn Under Quiet Magnetic Conditions

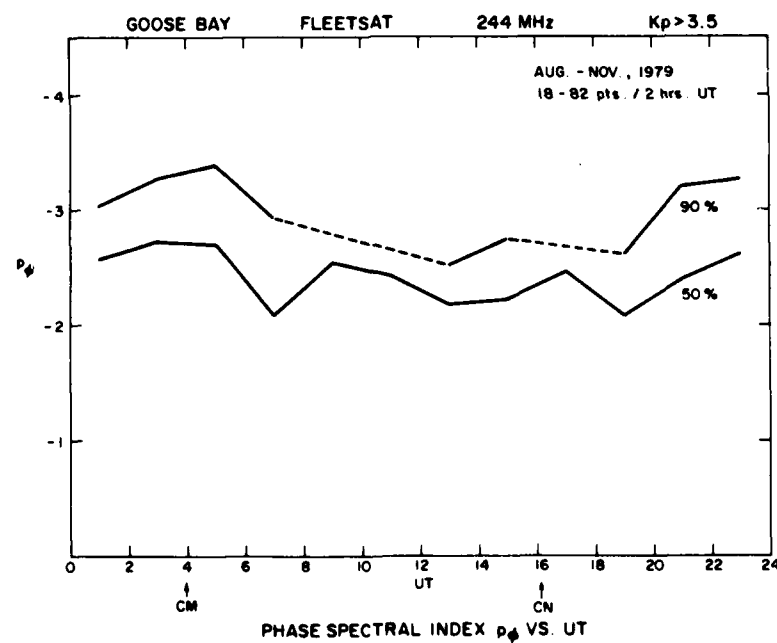


Figure 11b. Phase Spectral Index p_ϕ vs UT During the Autumn Under Disturbed Magnetic Conditions

4.2 Intensity Scintillation Statistics

4.2.1 SCINTILLATION INDEX S_4 DURING THE SPRING

The amplitude scintillation index S_4 obtained from Fleetsat data during Jan-Apr 1979, for magnetically quiet conditions ($K_p < 3.5$) is shown in Figure 12a with the corresponding data for magnetically disturbed ($K_p > 3.5$) conditions in Figure 12b. In the magnetically quiet case, the median curve peaks at $S_4 \sim 0.3$ between 06 and 08 UT while the 90th percentile curve shows a peak of $S_4 \sim 0.5-0.6$ also between 06 and 08 UT. The magnetically disturbed data for Jan-Apr (Figure 12b) shows a slight increase in the median level (peak $S_4 \sim 0.4$) between 02 and 04 UT with a second peak in the value of S_4 of about 0.4 between 08 and 10 UT. The 90th percentile curve shows a broad maximum of S_4 of about 0.6 between 02 and 08 UT.

Several differences between the amplitude and phase statistics should be noted. First, the daytime peak in σ_ϕ caused by bursts of FSK is hardly noticeable in S_4 . Second, the double humped nature of the nighttime behavior is well duplicated in S_4 but the median level during disturbed times increases only moderately as opposed to the large increase in σ_ϕ , caused most likely by increased drifts during magnetic storms. Unlike the phase scintillation values, the Fleetsat S_4 values during both quiet and disturbed times agree better with the scaled Wideband values for $60^\circ\Lambda$ (see Figures 82 and 84 in Report 1).

4.2.2 SCINTILLATION INDEX S_4 DURING THE SUMMER

Figures 13a and 13b illustrate the Fleetsat amplitude scintillation index S_4 observed in May-July 1979 for the magnetically quiet ($K_p < 3.5$) and disturbed ($K_p > 3.5$) cases respectively. Under quiet magnetic conditions (Figure 13a) the median level curve is flat at an S_4 of about 0.1 while the 90th percentile curve shows a nighttime plateau of about 0.25, dropping slightly in the daytime. Under disturbed magnetic conditions (Figure 13b) the median curve increases only slightly (peak S_4 about 0.25) at between 02 and 04 UT.

In this season also the scaled nighttime Wideband median data at $60^\circ\Lambda$ during quiet and disturbed times agrees well with the observed Fleetsat statistics (see Figures 89 and 90 in Report 1).

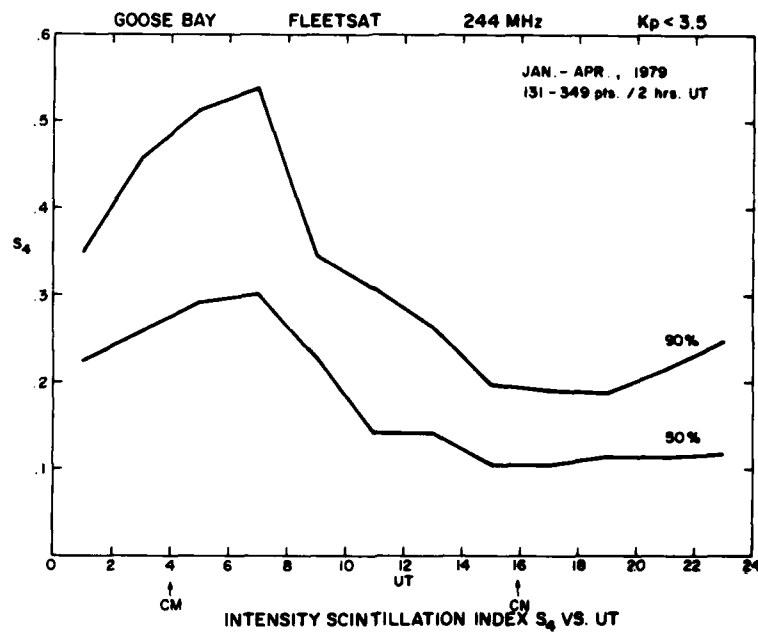


Figure 12a. Intensity Scintillation Index S_4 vs UT During the Spring Under Quiet Magnetic Conditions

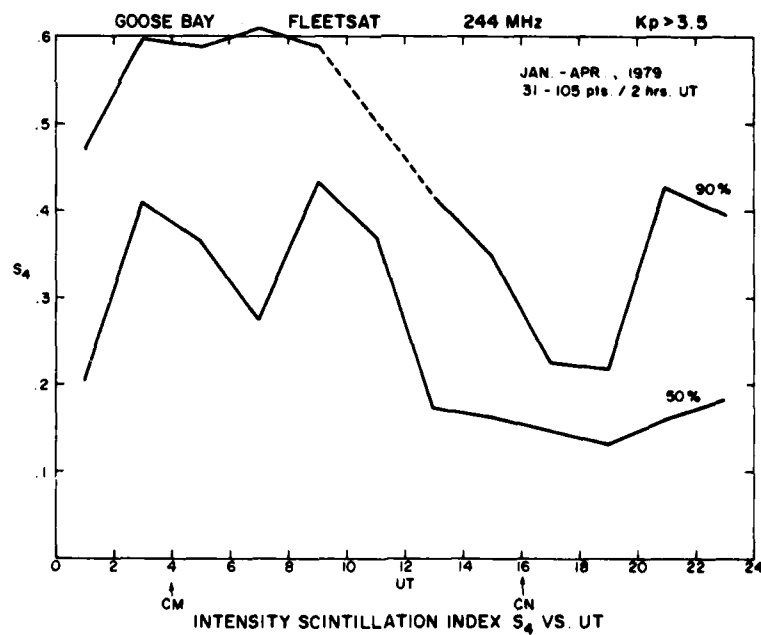


Figure 12b. Intensity Scintillation Index S_4 vs UT During the Spring Under Disturbed Magnetic Conditions

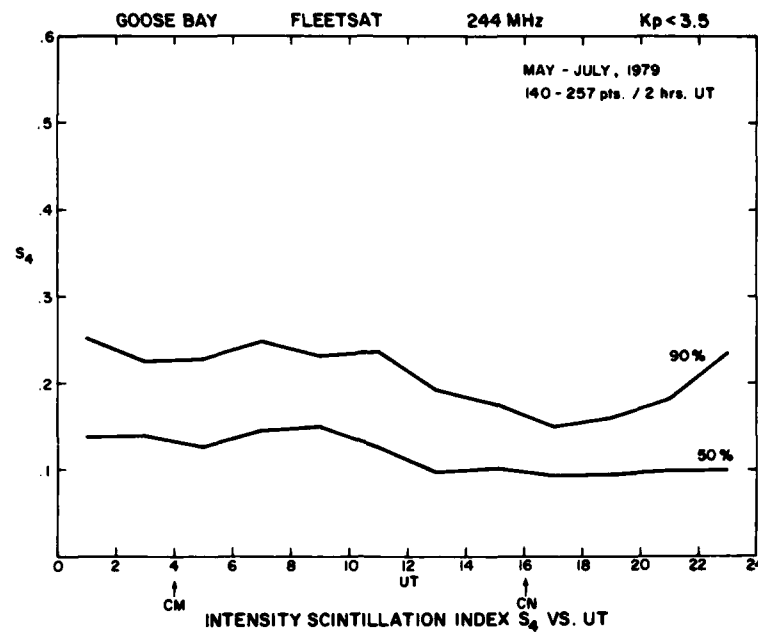


Figure 13a. Intensity Scintillation Index S_4 vs UT During the Summer Under Quiet Magnetic Conditions

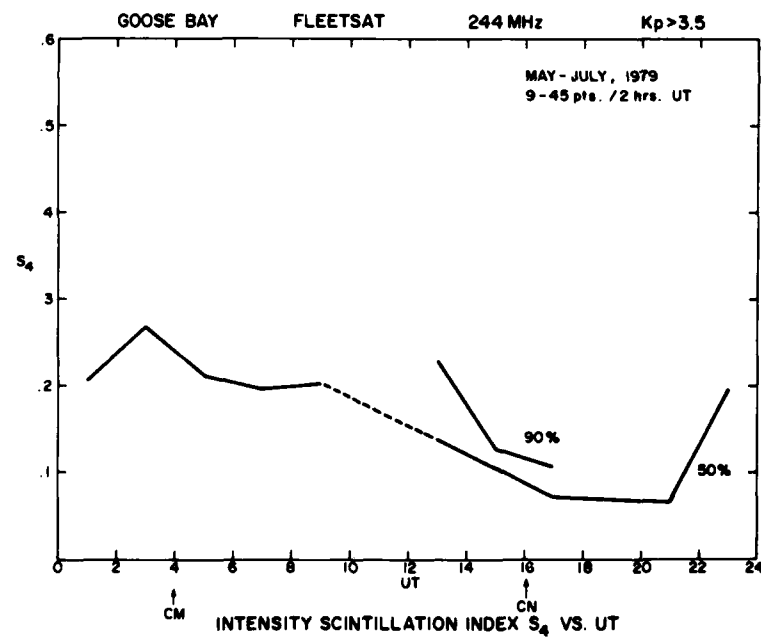


Figure 13b. Intensity Scintillation Index S_4 vs UT During the Summer Under Disturbed Magnetic Conditions

4.2.3 SCINTILLATION INDEX S_4 DURING THE AUTUMN

Figures 14a and 14b illustrate the Fleetsat amplitude scintillation index S_4 observed in Aug-Nov, 1979 for the magnetically quiet ($K_p < 3.5$) and disturbed ($K_p > 3.5$) cases respectively. Under quiet magnetic conditions (Figure 14a) the median level curve in S_4 is about 0.1 while the 90th percentile curve shows a night-time plateau in S_4 of about 0.2 decreasing in daytime to a value for S_4 of about 0.1. The magnetically disturbed data (Figure 14b) show a median peak in S_4 of about 0.3 between 02 and 04 UT with a 90th percentile peak in S_4 of about 0.45 between 04 and 06 UT.

It is interesting to note that the median level of S_4 is higher in the spring than in the autumn during both quiet and disturbed times. The summer S_4 median values fall between the spring and fall levels. These findings are consistent with the findings of Basu and Aarons³ (see Figures 4 and 5).

5. COMPARATIVE PHASE SPECTRAL STUDY OF CO-LOCATED WIDEBAND AND FLEETSAT DATA

It was pointed out in Section 4.1.5, that the average phase spectral slope p_ϕ obtained with Fleetsat data seemed consistently higher than the average p_ϕ obtained by the analysis of Wideband data. An opportunity to compare the two sets of p_ϕ within a common volume was obtained on 31 Mar 1979 (Day 90). The Wideband sub-ionospheric track in relation to the Fleetsat sub-ionospheric point for Goose Bay observations on this day has already been shown in Figure 1a. We show in Figure 15 the latitude variation of σ_ϕ as observed by Wideband on 138 MHz. The point of closest approach to Fleetsat is identified. A f^{-1} scaling of σ_ϕ values appropriate for 244 MHz is also shown by the dashed line. The large phase fluctuations are observed in the auroral oval between 63° and 66° latitude with the geometrical enhancement observed at the minimum Briggs-Parkin angle (BP on diagram) as discussed in Report 1.

The lower panel of Figure 15 shows the σ_ϕ as a function of UT as observed by Fleetsat. The highest σ_ϕ values are observed between 04 and 05 UT. It should be emphasized once more that Wideband gives a spatial snap-shot of the irregularity region whereas Fleetsat provides the temporal variation of both irregularity parameters and effective ionospheric drift at one fixed location.

This particular day (90) was moderately active magnetically. The K_p was 3^+ for 03-06 UT. These data were obtained during the quieting phase of a large magnetic storm that began with a Sudden Storm Commencement on 28 March and reached peak activity on 29 March. Fleetsat data and correlated particle precipitation using DMSP for 29 March will be discussed in Section 6. Moderate scintillation activity is noticed at the Fleetsat intersection (~ 2 rad) and the agreement between the scaled Wideband σ_ϕ and the 244 MHz σ_ϕ data is quite good.

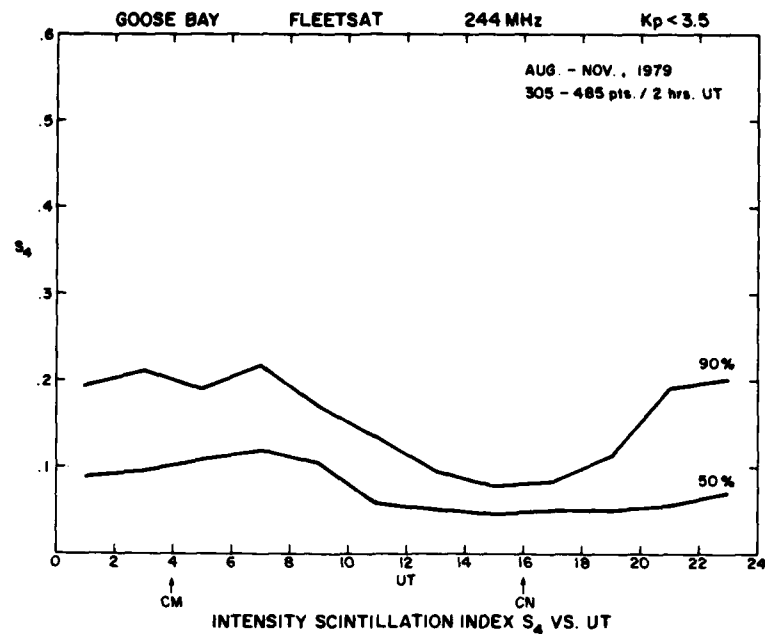


Figure 14a. Intensity Scintillation Index S_4 vs UT During the Autumn Under Quiet Magnetic Conditions

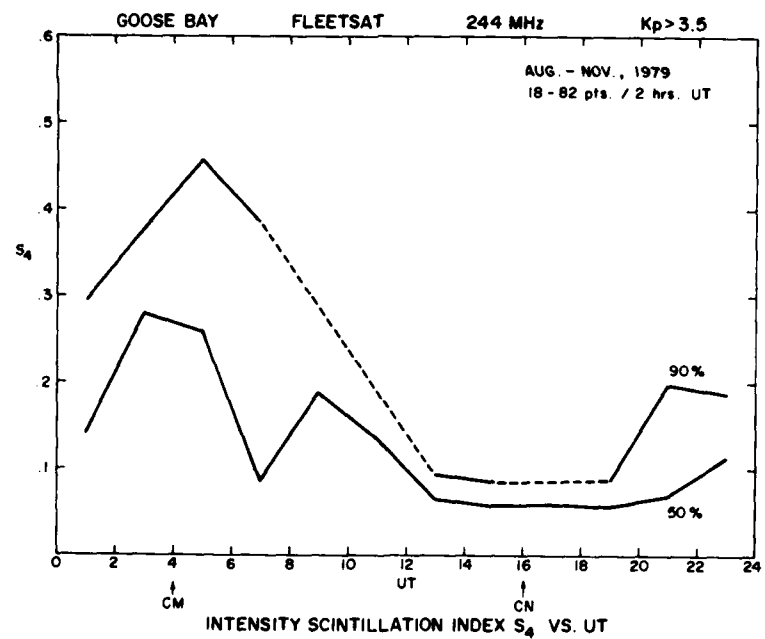


Figure 14b. Intensity Scintillation Index S_4 vs UT During the Autumn Under Disturbed Magnetic Conditions

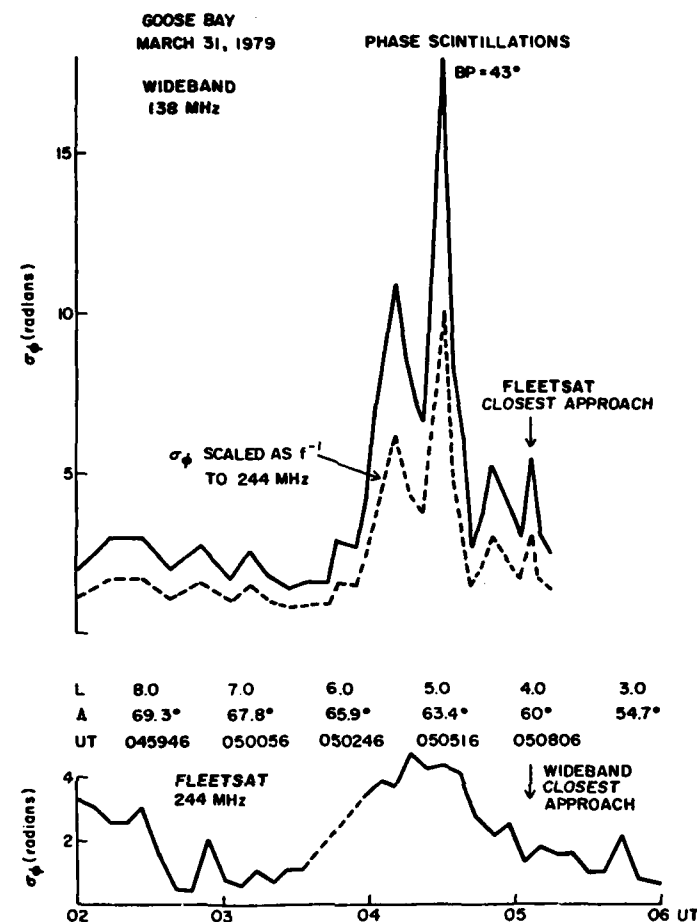


Figure 15. Comparison of Phase Scintillation Index σ_ϕ of Wideband (138 MHz) and Fleetsat (244 MHz) as Seen From Goose Bay, Labrador on 31 March 1979. Points of closest approach are marked

We also studied the phase spectra of the two data sets at the time when the subionospheric position of the Wideband satellite was closest to that of Fleetsat. These are shown in Figure 16 and the relevant parameters for some spectra contiguous to the time of closest approach, marked with asterisks, are shown in Table 1. A 20-sec sample with a 10-sec detrend ($f_c = 0.1$ Hz) is used for Wideband phase spectral analysis and the linear least squares fit of the slope is computed over 0.5 to 10 Hz. For Fleetsat a 400-sec sample with a detrend of 150 sec ($f_c = 0.0067$ Hz) is used and the slope is fitted over the range 0.025 - 0.5 Hz. The slope of -3.2 observed with Fleetsat is one unit larger than the -2.1 slope observed

for Wideband. We have already seen the same effect being observed for averages over large data ensembles as well as in Table 1. We shall discuss this point further in Section 7.

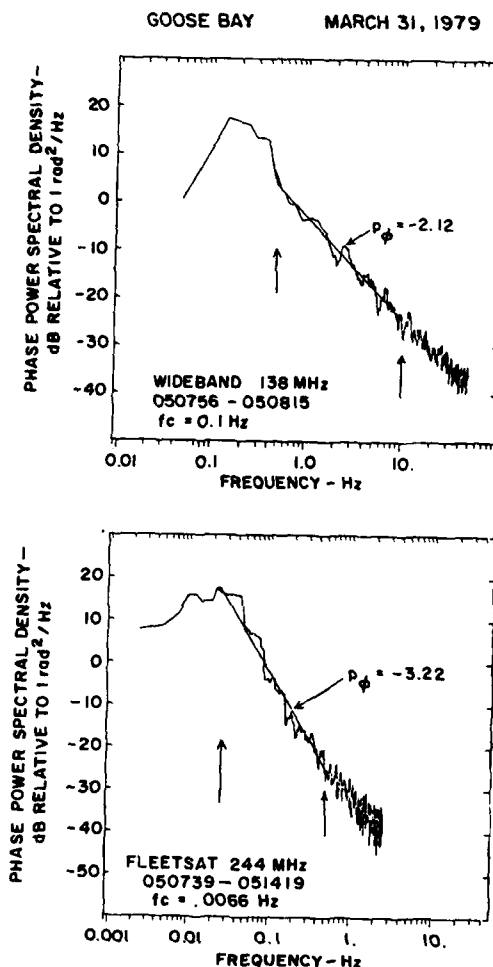


Figure 16. Comparison of Phase Spectral Index p_ϕ of Wideband (138 MHz) and Fleetsat (244 MHz) at the Time of Closest Approach of Wideband to the Fleetsat Intersection as Noted in Figure 15. The Wideband data uses a 20-sec sample with a 0.1 Hz detrend while the Fleetsat data uses a 400-sec sample with a 0.0067 Hz detrend

Table 1. Comparison of Phase Spectral Indices, Goose Bay,
31 March 1979

Fleetsat 244 MHz			Wideband 137 MHz		
UT	σ_{ϕ} Radians	P_{ϕ}	UT	σ_{ϕ} Radians	P_{ϕ}
045059	2.20	-2.86	050726	2.98	-2.08
045739	2.39	-2.60	050746	2.77	-2.02
050419	1.30	-2.35	*050806	4.95	-2.12
*051059	1.80	-3.22	050826	2.86	-2.13
051739	1.55	-2.93	050846	2.16	-2.20
Average $p_{\phi} = 2.8$			Average $p_{\phi} = 2.1$		

6. CORRELATED MEASUREMENTS OF PARTICLE PRECIPITATION FROM DMSP AND PHASE SCINTILLATIONS

Although relationships between charged particle precipitation and high latitude scintillations have been invoked for almost two decades (Herman,¹⁶ Aarons et al,¹⁷ and Frihagen¹⁸), there have been very few instances of simultaneous measurements of the two quantities (Weber and Buchau¹⁹). Martin and Aarons²⁰ and Aarons²¹ provided a comparison between DMSP (Defense Meteorological Satellite Program) photographs of auroral luminosity and scintillations. In this section we provide for the first time a detailed comparison of a DMSP energetic particle spectrum and coordinated phase and amplitude scintillation spectra.

The particle data used are those obtained from the DMSP/F2 satellite orbit 9380 in the evening MLT sector during a period of substorm activity. DMSP/F2 is a three-axis stabilized satellite in a nearly sun synchronous, circular orbit at an altitude of 840 km. The orbital period is 101 min; the nominal inclination is 98.75°. At launch the orbit was centered near the 0700-1900 meridian but it is subject to a very slow precessional drift toward later local times. The specific satellite orbit under study when mapped to 110 km altitude along magnetic field lines passed just 3° to the west of the Fleetsat intersection point as shown in Figure 17. The point of closest approach (CA) of DMSP at the latitude of Fleetsat intersection is indicated in the diagram. The pass occurred during a period of southward orientation of the interplanetary magnetic field (B_z negative) as shown in Figure 18a that caused a series of substorms as observed from the auroral electrojet index (AE) taken from Meng.²² It should be noted that this preliminary AE index, which is obtained

(Due to the large number of references cited above, they will not be listed here. See References, page 57.)

from North American magnetometer chains, cannot provide good coverage to monitor substorms between 18 and 04 UT due to the lack of observatories in the European longitude sectors. The middle panel of Figure 18a shows that the planetary index Kp was 6 at the time of the pass. On a more local level the DMSP pass occurred during the onset phase of a 400 γ negative bay which starts at 0152 UT on the Goose Bay magnetogram shown in Figure 18b. Unfortunately, the auroral photographs corresponding to this orbit are not available. However, we know from Figure 1b that at such disturbed times the statistical auroral oval should be in the vicinity of the Fleetsat intersection point.

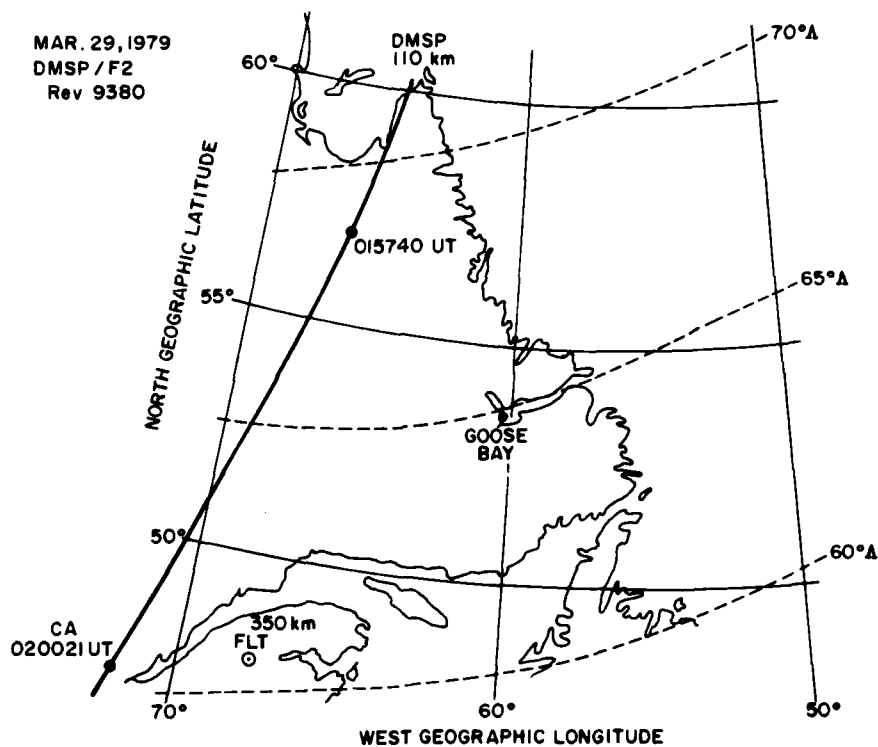


Figure 17. The DMSP/F2 Satellite Track Projected Along the Magnetic Field Line to 110 km for Orbit 9380 From Which Particle Data Were Obtained for the 29 Mar 1979 Study. This track is just 3° to the west of the Fleetsat intersection

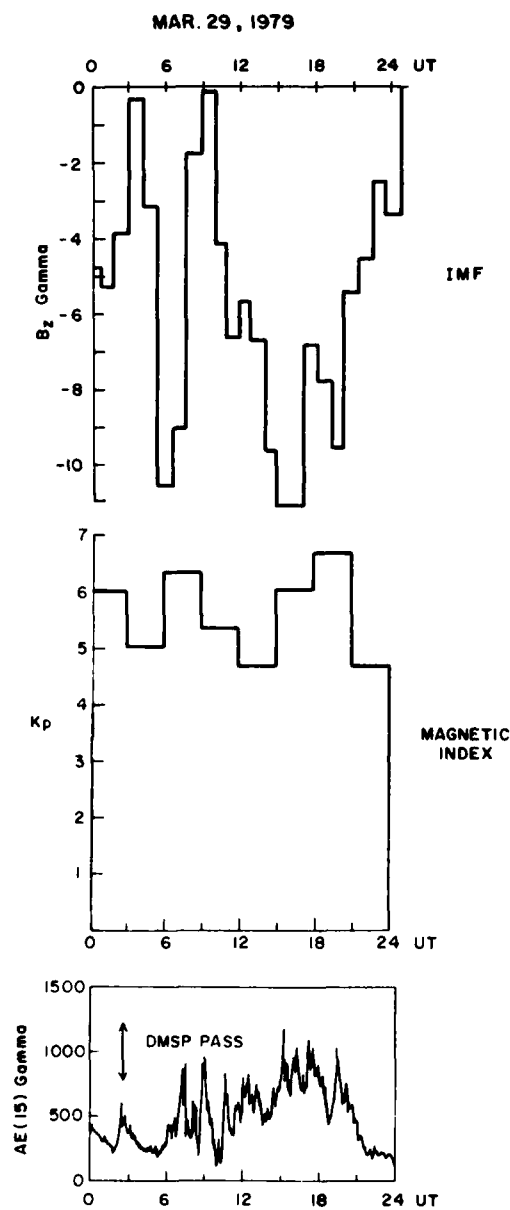


Figure 18a. The Interplanetary Magnetic Field B_z , Planetary Magnetic Index K_p , and Auroral Electrojet Index AE Data for 29 Mar 1979. The time of the DMSP/F2 pass is indicated

GOOSE BAY MAGNETOGRAM
MAR. 29, 1979
HORIZONTAL COMPONENT

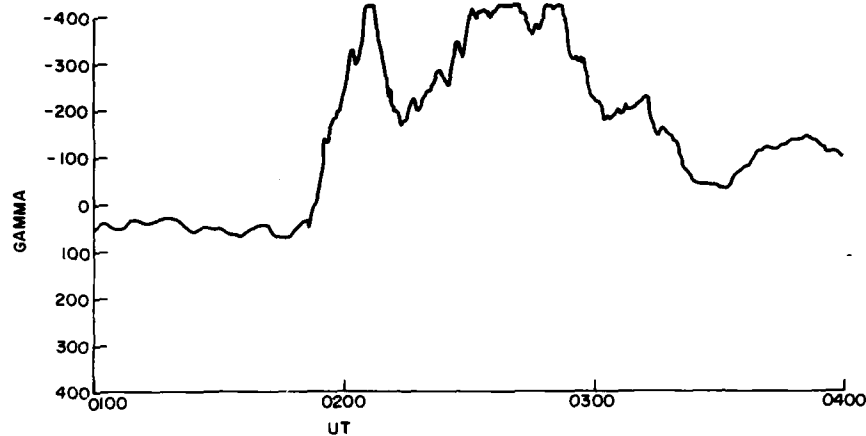


Figure 18b. The Horizontal Component of the Goose Bay Magnetogram on 29 Mar 1979 Showing a 400 γ Negative Bay

The DMSP particle detectors have been described in detail by Hardy et al.²³ The particle detector on DMSP/F2 consists of two curved plate electrostatic analyzers that measure the fluxes of electrons in 16 energy channels between 50 eV and 20 keV once per second. The apertures of the analyzers always face toward local vertical so that at auroral and polar cap latitudes they detect precipitating rather than backscattered and trapped electrons. One analyzer covers the energy range from 50 eV to 1 keV with a geometric factor of $4 \times 10^{-4} \text{ cm}^2 \text{ sr}$ and a $\Delta E/E$ of 10 percent. The other analyzer covers the energy range from 1 to 20 keV with a geometric factor of $4 \times 10^{-4} \text{ cm}^2 \text{ sr}$ and a $\Delta E/E$ of 12 percent. The large geometric factors insure that the flux level for the electrons in the diffuse aurora is well above the detector's sensitivity (Tanskanen et al.²⁴).

A synoptic view of the energetic electron measurements over the northern high latitudes for orbit 9380 is shown in Figure 19 and the point of closest approach to the latitude of the Fleetsat intersection at 020021 UT is identified as CA. We shall only discuss the evening part of the orbit which pertains to the coordinated

23. Hardy, D.A., Gussenhoven, M.S., and Huber, A. (1979) The Precipitation Electron Detectors (SSJ/3) for the Block 5D/Flights 2-5 DMSP Satellites: Calibration and Data Presentation, AFGL-TR-79-0210, ADA083136.

24. Tanskanen, P.J., Hardy, D.A., and Burke, W.J. (1981) Spectral characteristics of precipitating electrons associated with visible aurora in the premidnight oval during periods of substorm activity, J. Geophys. Res. 86:1379-1395.

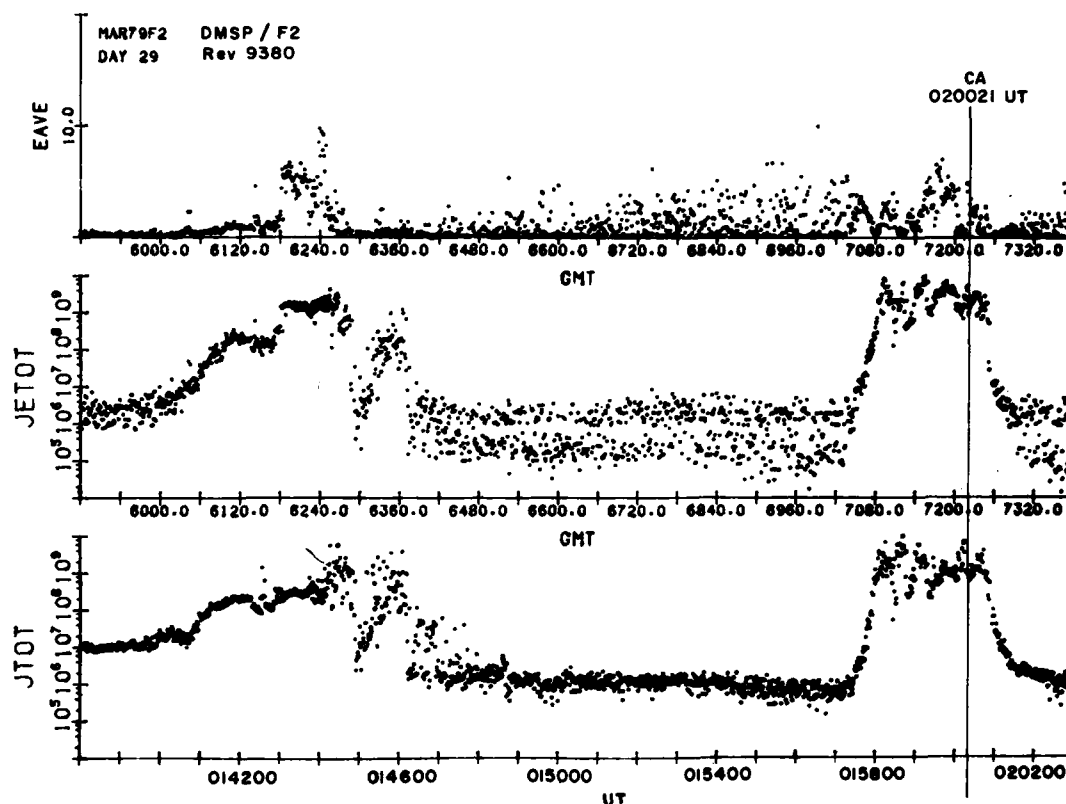


Figure 19. Energetic Electron Measurements Over the Northern Polar Cap for Orbit 9380 on 29 Mar 1979 (0130 - 0202 UT). Point of closest approach to the Fleetsat intersection latitude is marked as CA at 020021 UT

scintillation measurements. An enlarged view of the evening auroral oval precipitation region is shown in Figure 20. In both Figures 19 and 20 the particle data are plotted as JTOT, the directional integral flux ($\text{cm}^2 \text{sec sr}^{-1}$) in the bottom panel; JETOT, the directional energy flux [$\text{keV}(\text{cm}^2 \text{sec sr}^{-1})$] on the middle panel; and EAVE, the average energy in keV in the top panel. The scale for EAVE is linear. These quantities are plotted as functions of universal time UT, the geographic coordinates of the satellite GLAT and GLON, the corrected geomagnetic coordinates of the satellite mapped along the magnetic field line to 110 km MLAT and MLON, and the magnetic local time MLT. The poleward and equatorward boundaries of the oval were defined on the basis of JTOT exceeding the level of the polar rain or background respectively (Gussenhoven et al.²⁵). On this basis the equatorward

25. Gussenhoven, M.S., Hardy, D.A., and Burke, W.J. (1981) DMSP/F2 electron observations of equatorward auroral boundaries and their relationship to magnetospheric electric fields, *J. Geophys. Res.* 86:768.

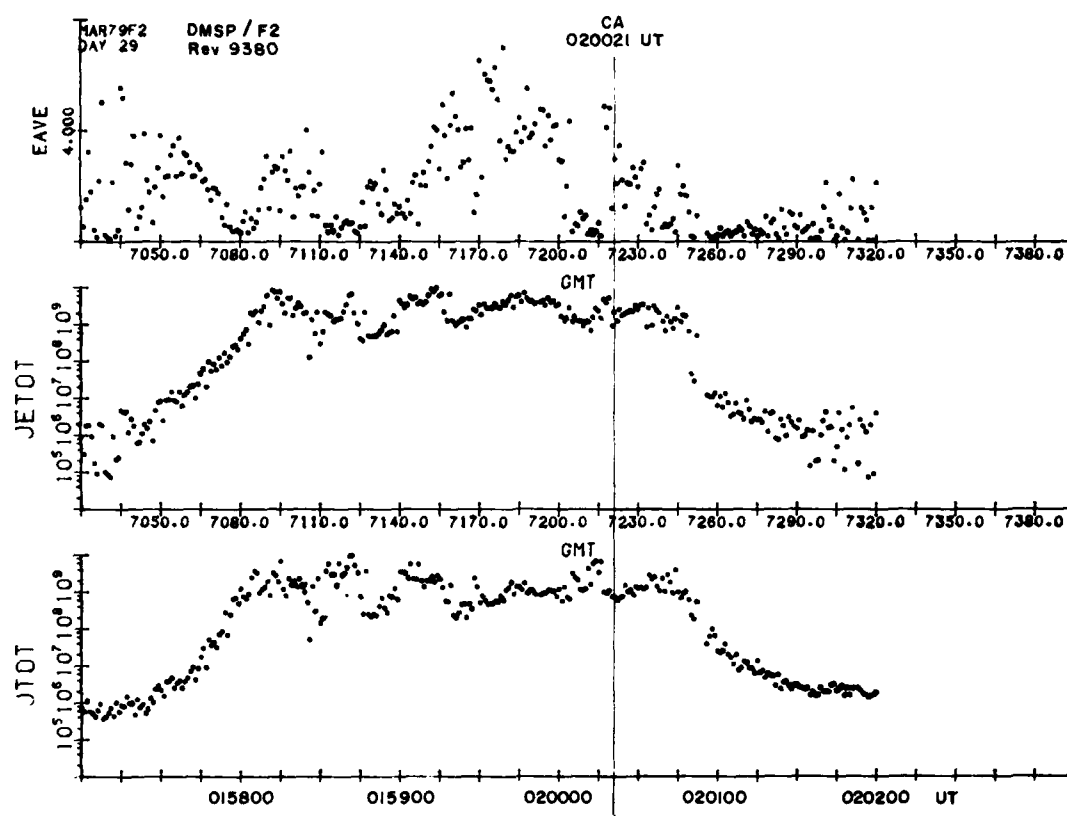


Figure 20. Enlarged View of the Evening Auroral Oval Precipitation Region for Orbit 9380 on 29 Mar 1979 (0157 - 0202 UT)

boundary of the aurora in the evening sector is at $59^\circ\Lambda$ (at the 110 km level) which for $K_p = 6$ matches well with the empirical relationship $\Lambda_{CGM} = 71.2 - 2.1 K_p$ developed by Gussenhoven et al.²⁵ for the northern hemisphere evening boundary.

From Figure 20, we see that the Fleetsat intersection is within the evening precipitation region. Moreover, from the nature of the average energy of the precipitating fluxes (about 4 keV) the intersection point is within the region of the diffuse aurora. In the absence of simultaneous DMSP photographs it is difficult to establish the exact width of the diffuse aurora, but based on the shape of the electron spectra and their average energy, it is likely that the entire latitude range spanned by the satellite between 0159 and 0201 UT can be considered to be within the diffuse auroral precipitation region. Within that interval, at least two relatively narrow regions of significant flux enhancements are observed in conjunction with decrease of the average energy (020015 and 020040 UT). The number flux and the electron flux show significant fluctuation in the two regions reaching values as high as

8×10^9 electrons $(\text{cm}^2 \text{ sec sr})^{-1}$ and 3×10^9 keV $(\text{cm}^2 \text{ sec sr})^{-1}$ respectively. The average energy of this particle population is about 400 eV for the first region and about 1 keV for the second, whereas the surrounding regions have typical energies on the order of 3 keV.

To show the particle spectra in the vicinity of the point of closest approach, we present a series of three plots each showing ten differential energy spectra for ten successive seconds starting at 015950, 020010, and 020030 in Figures 21a, 21b, and 21c respectively. The first one (Figure 21a) obtained poleward of the Fleetsat intersection, when taken in conjunction with the relevant portion of Figure 20, shows smooth variations in JTOT, JETOT, and EAVE and a quasi-thermal spectrum. The EAVE reaches a maximum value of 5 keV at 015952 UT. A drastic change in spectral shape occurs in Figure 21b particularly during 020010-020016 UT.

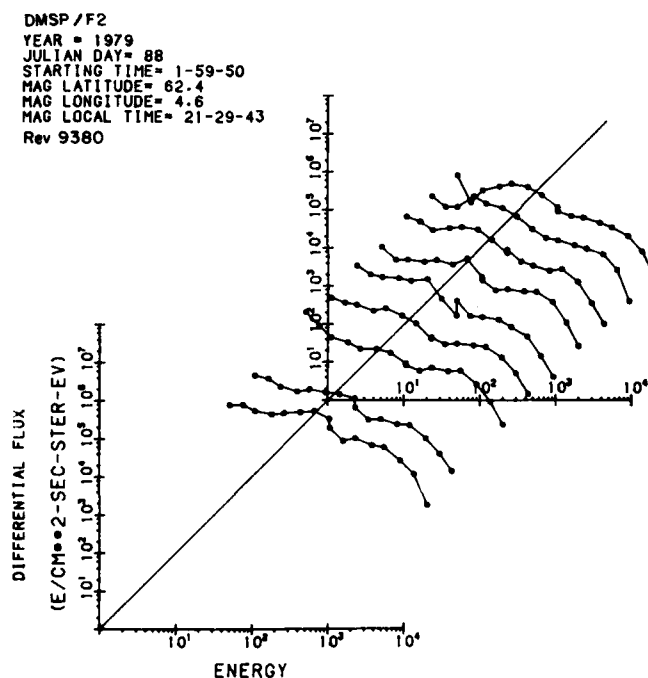


Figure 21a. Ten differential Energy Spectra for Ten Successive Seconds of DMSP Precipitating Electron Data Taken From Orbit 9380 on 29 Mar 1979 Poleward of the Fleetsat Intersection Between 015950-015959 UT Showing Smooth Variations in JTOT, JETOT, and EAVE and a Quasi-thermal Spectrum

DMSP/F2
 YEAR = 1979
 JULIAN DAY = 88
 STARTING TIME = 2-0-10
 MAG LATITUDE = 61.3
 MAG LONGITUDE = 3.7
 MAG LOCAL TIME = 21-26-14
 Rev 9380

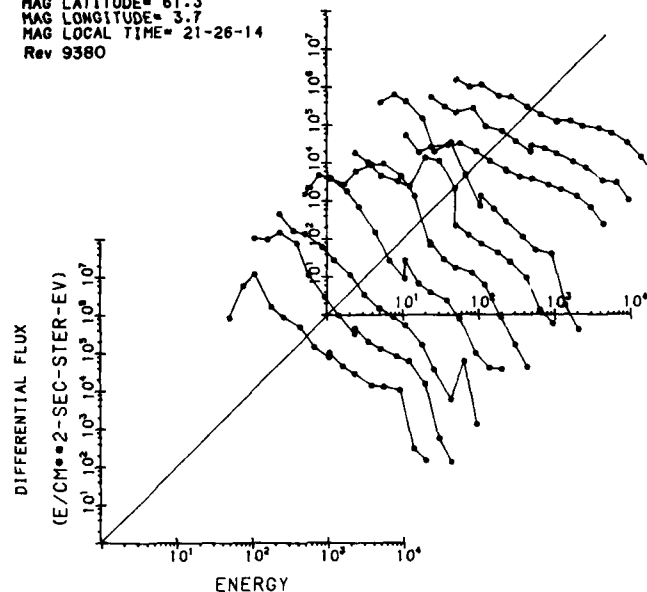


Figure 21b. Same as in Figure 21a but Showing Decrease in High Energy Flux and Increase in Lower Energies Between 020010 - 020019 UT

There is a large increase in flux at the lower energies with a corresponding decrease in flux at the higher energies leading to a severe reduction in the average energy as mentioned earlier. Further, low-energy peaks in the range 100-600 eV are found to be superimposed on the basically quasi-thermal background distribution. Such spectra were also shown by Tanskanen et al²⁴ to exist in a similar region of the nighttime auroral oval. The spectra observed between 020020 and 020029 UT are very similar to those observed between 020017 and 020019 UT and are therefore not shown. In Figure 21c, near the second region identified with low average energy in Figure 20, we find that the irregular peaks at the low energy end have mostly disappeared and have been replaced by fluxes which increase monotonically with decreasing energy of measurement, down to the lowest energy, namely 47 eV. Some of the spectra show that the low energy component can exceed $10^7 \text{ (cm}^2 \text{ sec sr eV)}^{-1}$ at energies $< 100 \text{ eV}$ and most of the spectra can be described by power law shapes up to energies of about 10 keV.

DMSP/F2
 YEAR = 1979
 JULIAN DAY = 88
 STARTING TIME = 2-0-30
 MAG LATITUDE = 60.3
 MAG LONGITUDE = 2.8
 MAG LOCAL TIME = 21-23-4
 Rev 9380

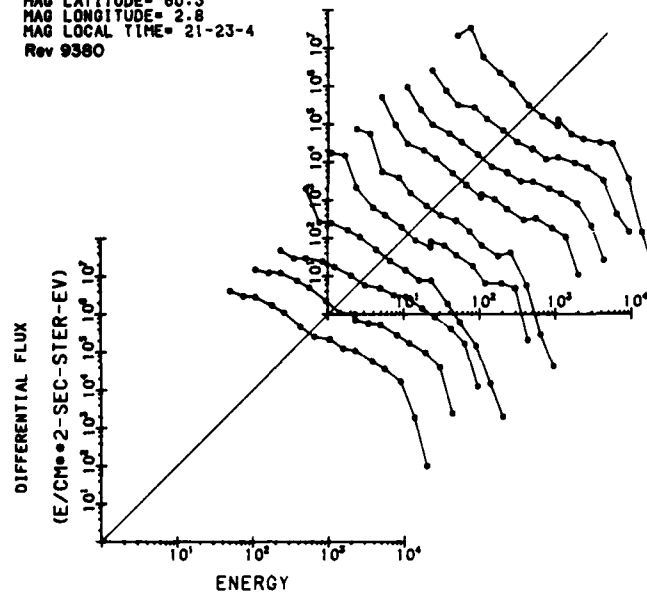


Figure 21c. Same as in Figure 21a but Showing Monotonic Increasing Fluxes With Decreasing Energy Down to 47 eV Between 020030 - 020039 UT

To study the latitudinal variation of this low-energy component, we show in Figure 22 plots of differential fluxes of the three lowest energy channels as a function of the position of the satellite. The behavior of a higher energy channel, namely the 5.5 keV flux, is also shown to give some idea of the relative change in particle spectrum near the equatorward edge of the diffuse aurora. We find two distinct regions centered near 020010 and 020040 UT of width approximately one-half degree of latitude where there are intense fluxes [10^7 electrons/(cm² sec sr eV)] of precipitated low-energy electrons. In these regions, particularly in the first one, there is a corresponding decrease of the high energy flux indicating perhaps that the low energy fluxes are enhanced at the expense of the high energy ones. The latitudinal widths of the low energy precipitation regions are reminiscent of the F-region 'blobs' observed at Chatanika which were found to be associated with scintillation enhancements using the Triad satellite.²⁶

26. Vickrey, J.F., Rino, C.L., and Potemra, T.A. (1980) Chatanika Triad observations of unstable ionization enhancements in the auroral F-region, Geophys. Res. Lett. 7:789.

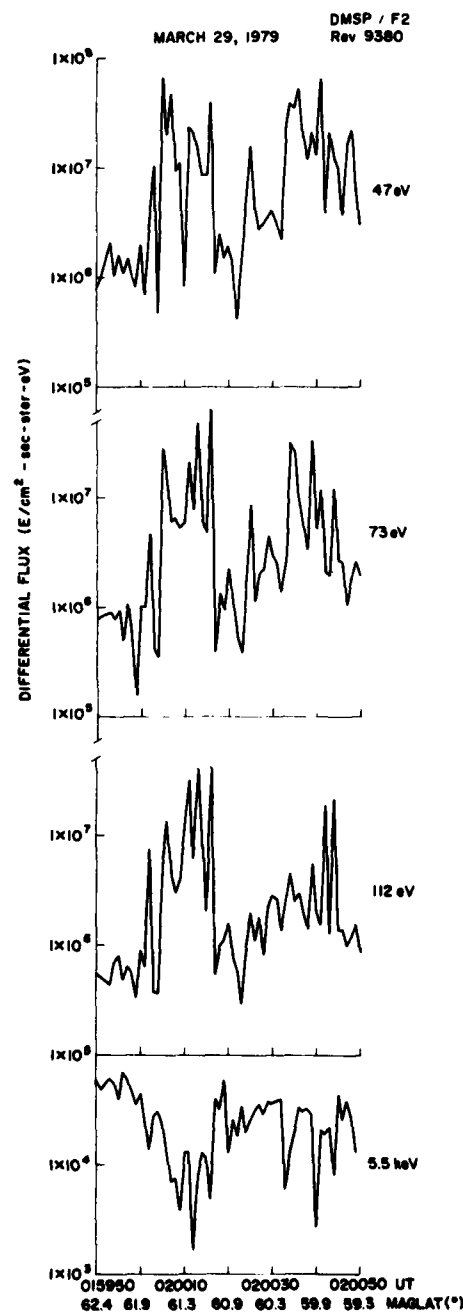


Figure 22. Differential Flux Measurements of the 47, 73, 112 keV and 5.5 keV Energy Channels From Orbit 9380 Showing the Change in Particle Spectrum With Latitude

Total electron content (TEC) measured from Goose Bay using the polarimeter technique and transmissions from ATS-5 at 137 MHz are shown in Figure 23. The TEC exhibits significant enhancement at 0152 UT which is about 8 min prior to the passage of the DMSP satellite through the same latitude region. These measurements refer to a sub-ionospheric position of 48.34°N and 61.91°W. It is important to note that the TEC enhancement is observed at the time of onset of a negative bay in the Goose Bay magnetogram as shown in Figure 18b. The TEC enhancement reaches its peak value at 0158 UT which is very close to the time of the DMSP pass.

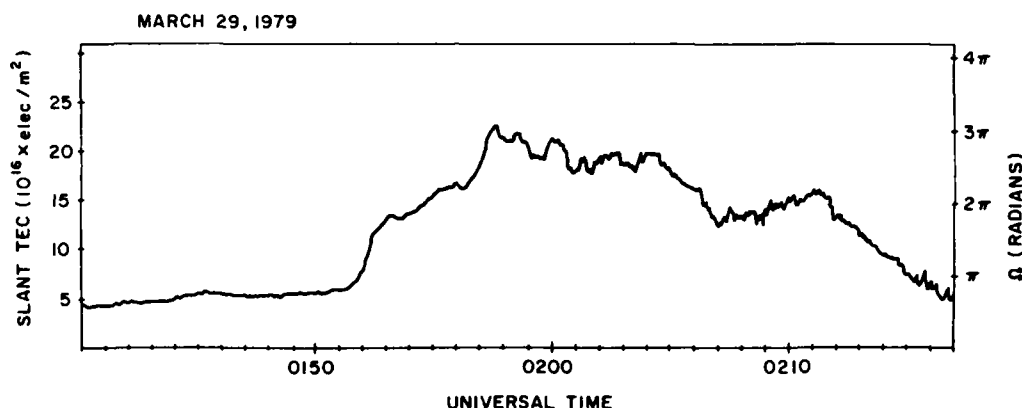


Figure 23. Total Electron Content (TEC) Measurements From the ATS-5 Satellite Measured at Goose Bay, Labrador on 29 Mar 1979 Showing Onset of TEC Increase at Approximately 0150 UT

The time record of phase and amplitude fluctuations of Fleetsat signal at 244 MHz after detrending with a filter cutoff of 0.0067 Hz for the same period shown in Figure 24 exhibits a large increase in both quantities at almost exactly the time of the TEC increase registered by ATS-5. A similar situation was discussed by Aarons²¹ for the 31 October 1972 storm. Since the ionospheric intersection points of ATS-5 and Fleetsat are separated by 6° of longitude, it is obvious that low-energy electrons were precipitating in the vicinity of 60°N over a relatively wide swath of longitudes. The almost simultaneous response of the magnetogram (which is a signature of ionospheric currents and their motion) and phase and amplitude scintillations (which respond to ionospheric irregularities) to the particle influx raises important questions regarding irregularity generation mechanisms and growth times for large amplitude irregularities. On the other hand, modeling studies have shown that the background F-region requires tens of minutes to reach diffusive

GOOSE BAY 29 MAR 1979

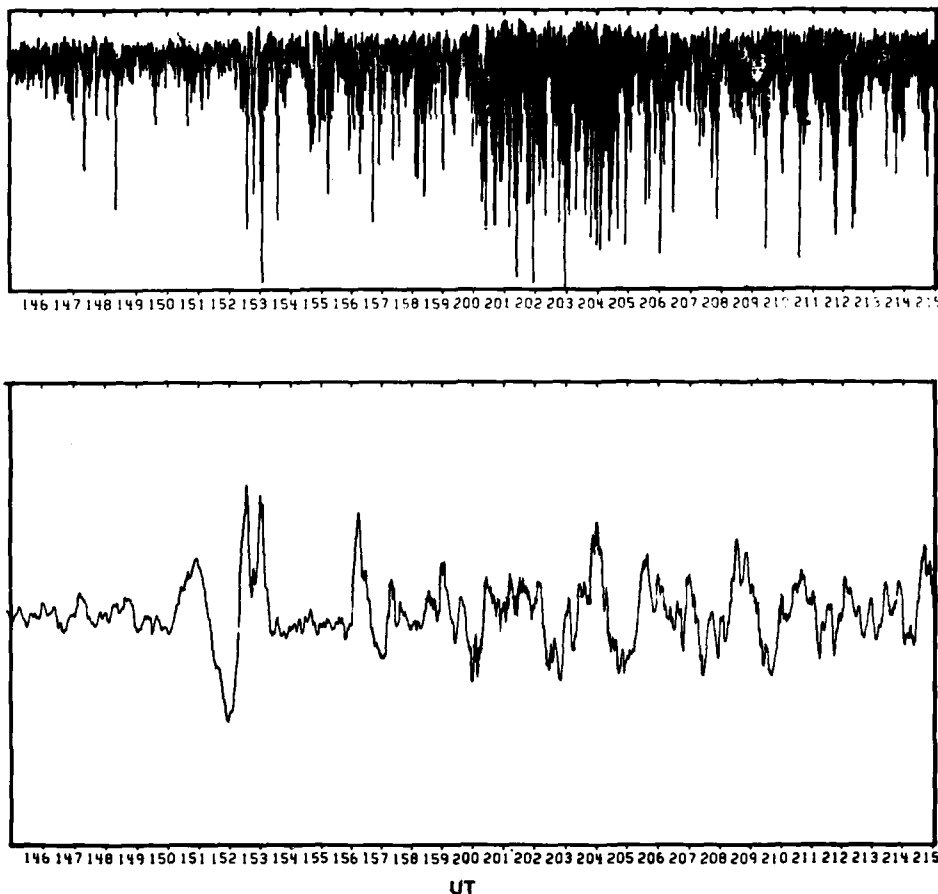


Figure 24. Time Record of Phase and Amplitude Fluctuations of Fleetsat From Goose Bay on 29 Mar 1979 Detrended With a Filter Cutoff of 0.0067 Hz

equilibrium in response to this energy input (Roble and Rees,²⁷ Watkins and Richards²⁸). These authors show that during this time the shape of the F-region undergoes marked changes which could very well be responsible for the immediate effect seen on the polarimeter in Figure 23. Further, since the F-peak decays slowly the density remains a factor of 2 larger than the pre-auroral density 1 h after the auroral

27. Roble, R.G., and Rees, M.H. (1977) Time-dependent studies of the aurora: effects of particle precipitation on the dynamic morphology of ionospheric and atmospheric properties, Planet. Space. Sci. 25:991.

28. Watkins, B.J., and Richards, P.G. (1979) A theoretical investigation of the role of neutral winds and particle precipitation in the formation of the auroral F-region ionosphere, J. Atmos. Terr. Phys. 41:179.

event occurs. Thus a net electron density increase at F-region heights exists in the nighttime ionosphere as a result of the auroral event. This is an important result which has a significant bearing on the subsequent behavior of scintillations.

The time history of amplitude and phase scintillation indices S_4 and σ_ϕ during a 3-h period commencing at 0100 UT on 29 Mar 1979 is shown in Figure 25. Corresponding phase spectral strength parameter T_ϕ and slope p_ϕ are shown in the lower two panels. The rather dramatic increase of σ_ϕ at 0150 UT from 2 to 14 rad is accompanied by a 3-fold increase in amplitude scintillation index from 0.2 to 0.6. If we assume that the above range of S_4 index is within the weak scatter limit, then we can study the variation of the σ_ϕ/S_4 ratio prior to 0150 UT and thereafter. While the average value of this ratio is 14 before the onset of severe phase scintillations, the average value of the ratio doubles to 28 between 0152 UT and 0325 UT. This ratio could reflect a change in anisotropy (Rino,¹² Fremouw²⁹) or an increase in the effective ionospheric E-W drift velocity in response to the substorm. It has been discussed in Section 4 that increased drifts can result in large phase scintillations with a fixed detrend if the source is a geostationary satellite. Because of the low elevation of the observations, it is difficult to visualize a plausible change in the anisotropy which could account for the doubling of the σ_ϕ/S_4 ratio. Thus the second alternative becomes more plausible particularly because Chatanika drift measurements during substorms have shown large increases in the ion drifts at the same invariant latitudes as these measurements.³⁰

The spectral intensity T_ϕ in general follows the behavior of σ_ϕ except near 0225 UT when σ_ϕ increases to a peak of 17 rad without the increase being reflected in T_ϕ , the spectral intensity at 1 Hz. This is possible when there is only a low frequency enhancement in the spectrum if p_ϕ does not vary considerably. The p_ϕ values generally vary between 2.5 and 3 and are in general larger than the average Wideband p_ϕ values as discussed in the case study presented in Section 5. Two typical samples of phase spectra are shown in Figures 26a and 26b. The phase spectra are described by uniform power law types with spectral indices varying between 2.5 and 3 as mentioned earlier.

29. Fremouw, E. J. (1980) Geometrical control of the ratio of intensity and phase scintillation indices, *J. Atmos. Terr. Phys.* 42:775.

30. Foster, J. C., Doupnik, J. R., and Stiles, G. S. (1981) Ionospheric convection and currents in the midnight sector on November 8, 1979, *J. Geophys. Res.* 86:2143.

GOOSE BAY MAR. 29, 1979

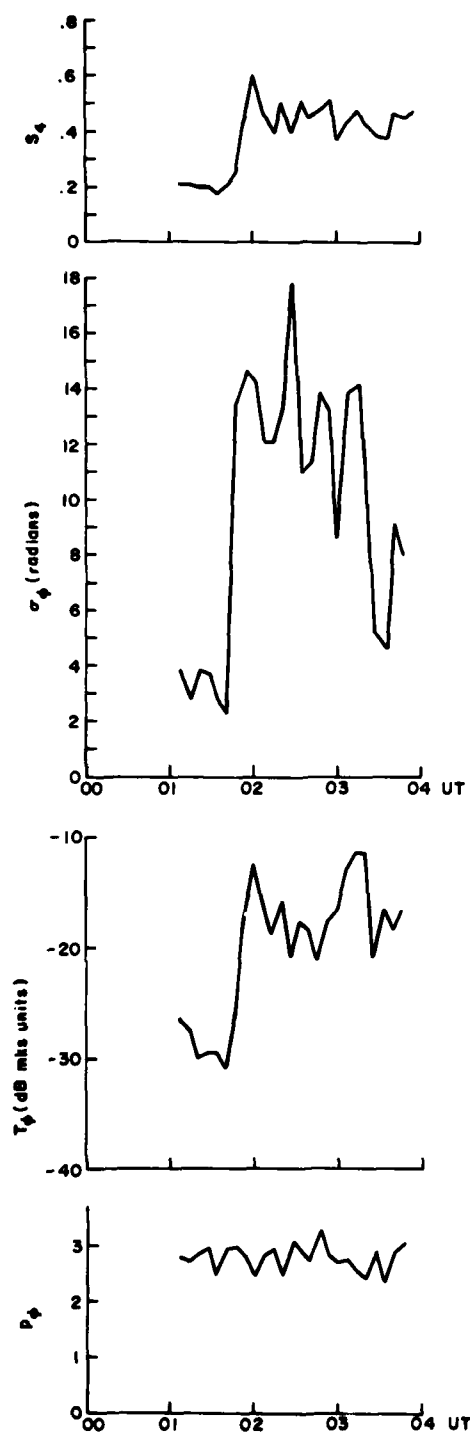


Figure 25. Intensity and Phase Scintillation Parameters S_4 , σ_ϕ , T_ϕ and p_ϕ of Goose Bay FLEETSAT on 29 Mar 1979 (01-04 UT)

GOOSE BAY MAR. 29, 1979

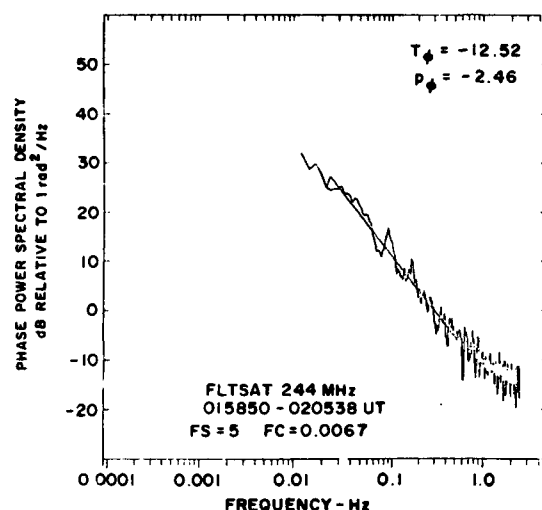


Figure 26a. Sample Power Spectrum of Phase Scintillation on 29 Mar 1979, 015850-020538 UT at a Time When $\sigma_\phi = 14.3$ rad. The sampling frequency $f_s = 5$ Hz and the detrend frequency $f_c = 0.0067$ Hz

GOOSE BAY MAR. 29, 1979

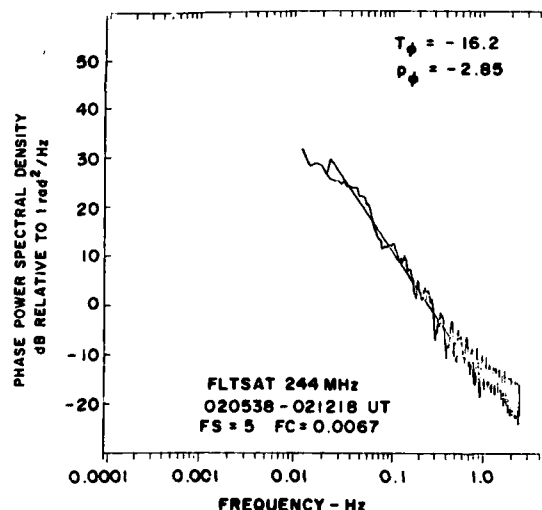


Figure 26b. Sample Power Spectrum of Phase Scintillation on 29 Mar 1979, 020538-021218 UT at a Time When $\sigma_\phi = 12.08$ Rad. The sampling frequency $f_s = 5$ Hz and the detrend frequency $f_c = 0.0067$ Hz

The corresponding amplitude spectra are shown in Figures 27a and 27b. To study the variation of the Fresnel frequency with increasing drift speed, we have superimposed on Figure 27a the amplitude spectrum obtained between 0132-0138 UT on 29 Mar, prior to the onset of the large phase fluctuations. The two spectra look very similar with the one corresponding to the larger S_4 index being raised almost

a decrease in spectral intensity above the one for the weaker scintillations. Both have their Fresnel frequencies between 0.2 and 0.3 Hz. Thus it is not possible to use the Fresnel frequency criterion to distinguish spectral differences between spectra whose σ_ϕ/S_4 ratio differ by a factor of 2. However, in Figure 2 we have superimposed the intensity spectra obtained between 045419 and 050059 UT on 31 Mar 1979, during the event that was discussed in Section 5. The average σ_ϕ/S_4 ratio of the Fleetsat data listed in Table 1 for 31 Mar is approximately 4 even though the S_4 level of both spectra are the same. We have already mentioned that the σ_ϕ/S_4 ratio of the 29 Mar data shown in Figure 27b is 28. Thus there is a factor of 7 difference in the σ_ϕ/S_4 ratios of the two spectra shown in Figure 27b. We do indeed find a great difference in the spectral character of the two samples. The 31 Mar sample has a Fresnel frequency of 0.04 Hz whereas the 29 Mar data shows a roll-off between 0.2 to 0.3 Hz. Since the Fresnel frequency is directly proportional to the effective drift velocity, we have further evidence that increased drift velocities contributed to the increase in the σ_ϕ/S_4 ratio during the magnetic disturbances observed on 29 Mar 1979.

It should be pointed out here that the slopes of the intensity spectra are rather shallow in comparison to the phase spectra. Further studies will be made by using a higher sampling frequency so that we can explore the high frequency roll-off portions of the spectra better. Such a study is particularly important for the high-velocity samples where the Fresnel frequencies are found to be greater than 0.1 Hz.

7. CONCLUSIONS

Phase and amplitude scintillations at 244 MHz using a geostationary satellite as a source have been presented for a 10-month period in 1979. The observing station was Goose Bay, Labrador, which puts the ionospheric intersection at $60^\circ\Lambda$, which is within the mid-latitude trough for quiet magnetic conditions. As opposed to the sun-synchronous Wideband satellite study presented in Report 1, the geostationary source made complete diurnal coverage possible. However, in keeping with earlier intensity scintillation studies in this region,³ it was found that median nighttime phase perturbations during magnetically quiet periods were generally below 2 rad with a maximum activity of 5 rad during the premidnight period in the spring. Thus no major propagation problems are expected in UHF systems operating through such an environment.

Magnetic storms, on the other hand, are sometimes accompanied by relatively larger increases of phase scintillation than amplitude scintillations. This was interpreted as most probably resulting from an increase in the effective drift velocity during magnetic storms. It is well known that the N-S component of the auroral

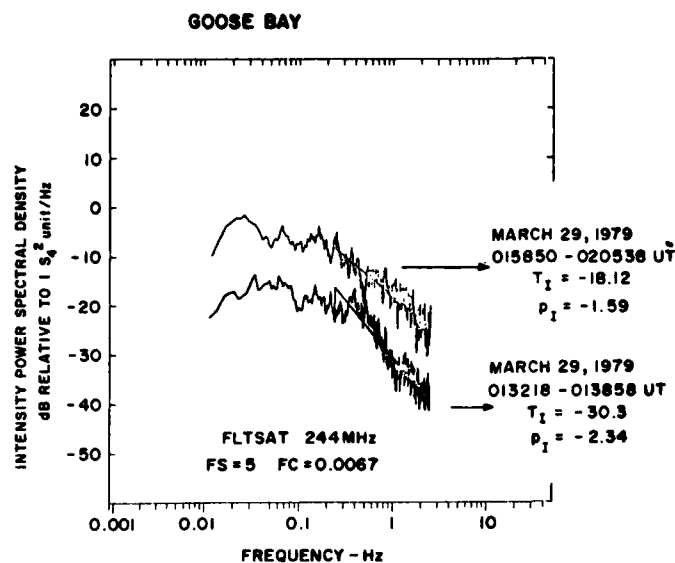


Figure 27a. Sample Power Spectra of Amplitude Scintillation on 29 Mar 1979 Between 015850 and 020538 UT With $S_4 = 0.60$ and Between 013218 and 013858 UT With $S_4 = 0.18$ Showing Similar Values of the Fresnel Frequency

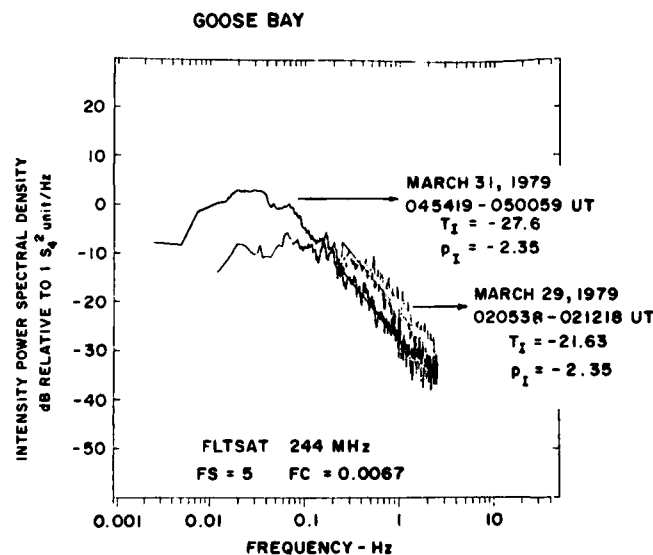


Figure 27b. Same as in Figure 27a but for 29 Mar 1979 Between 020538 and 021218 UT With $S_4 = 0.46$ and 31 Mar 1979 Between 045419 and 050059 UT With $S_4 = 0.51$ Showing Very Different Values of the Fresnel Frequency

electric field is greatly enhanced during storms giving rise to large plasma drifts in the E-W direction. Thus, as a result of the larger irregularity amplitude caused by the equatorward motion of the auroral oval and the attendant increased drift velocity during such times, it is possible for UHF systems to suffer phase perturbations in excess of 10 rad (with $f_c = 0.0067$ Hz) without the S_4 index being driven into saturation.

A feature of considerable scientific interest that became evident as a result of this study is that the observed phase spectral index p_ϕ of the Fleetsat data base is consistently larger than the p_ϕ of the Wideband data discussed in Report 1. This was found to be true statistically as well as for the case study in which the Fleetsat and Wideband satellite transmissions were received through a co-located volume. The Fleetsat spectral slopes p_ϕ are generally computed at scale lengths somewhat shorter than the corresponding ones for Wideband. It needs to be established whether a larger p_ϕ value in the Fleetsat case is indicative of a steeper irregularity spectral index at smaller scale lengths. In this connection, it may be mentioned that in the equatorial region, the one-dimensional spectral index of the in-situ data is shallow (about 1.5) for scale lengths larger than a kilometer and steep (approximately 3) for smaller scale lengths (Rino et al,³¹ Basu et al³²). High resolution in-situ data from AE-D is currently being studied to investigate the existence of such dual slopes in auroral irregularities. It is also interesting to note that 2-dimensional simulation of somewhat larger scales of auroral irregularities (approximately 2.5 km) has shown that the spectral index in the N-S direction is shallower than the index found in the E-W direction.³³ If the simulation results imply a separable form for irregularity power spectral density functions in the N-S and E-W directions, an alternative explanation for the difference in spectral indices can be put forward. This is because the temporal structure of Wideband scintillation arises from the satellite motion primarily in a N-S direction whereas the structure of Fleetsat scintillations is caused by ionospheric E-W motion. Thus a further study of the simulation results regarding the cause of such spectral differences seems to be warranted.

Finally, a case study of magnetic storm induced particle precipitation and scintillations was presented. We were able to show that the scintillations in the diffuse auroral region at the equatorward edge of the auroral oval were well correlated with intense fluxes of low-energy electrons of latitudinal widths of approximately one-half to 1° and longitudinal width exceeding 10°. The increase in measured TEC and the intensification of phase and amplitude scintillations

31. Rino, C.L., Tsunoda, R.T., Petricek, J., Livingston, R.C., Kelley, M.C., and Baker, K.D. (1981) Simultaneous rocket-borne beacon and in-situ measurements of equatorial spread-F - Intermediate wavelength results, J. Geophys. Res. 86:2411.
32. Basu, Sunanda, Basu, S., McClure, J.P., Hanson, W.B., and Whitney, H.E. (1982) High resolution topside in-situ data of electron densities and VHF/GHz scintillations in the equatorial region, J. Geophys. Res. (in press).
33. Keskinen, M.J., and Ossakow, S.L. (1982) Nonlinear evolution of plasma enhancements in the auroral ionosphere, 1: Long wavelength irregularities, J. Geophys. Res. 87:144.

were simultaneous. It is interesting to note that Buchau et al³⁴ found that during low sunspot years even active auroral conditions failed to produce enhanced scintillations at 250 MHz when the ray path passed near discrete forms embedded in diffuse aurora near the equatorward edge of the oval. Thus further studies are needed to establish whether the intense low energy precipitation and enhanced scintillations in this region discussed in this report are related to the current solar maximum.

The data from the DMSP thermal plasma monitor³⁵ is currently being examined to study the ion density and temperature behavior in the precipitation region near the Fleetsat intersection point. The preliminary ion density analysis presented in Figure 28 shows that the low-energy precipitation near 0200 UT is accompanied by density enhancements and sharp gradients at 840 km. Densities at this altitude are found to be in excess of $10^5/\text{cm}^3$ which seems also related to the high sunspot conditions (Rich,³⁶ Rino and Vickrey,³⁷ see their Figure 10). This provides a clear link between latitudinally narrow bands of precipitation and topside F-region density enhancement which has been postulated in many recent studies (Vickrey et al,²⁶ Rino and Vickrey,³⁷ and Tsunoda and Vickrey³⁸).

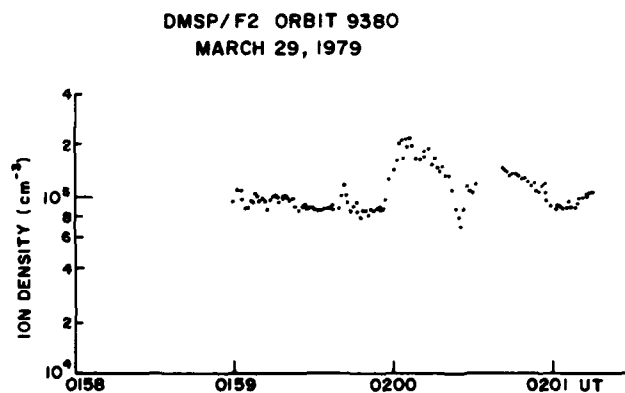


Figure 28. Ion Density Measurements From the DMSP/F2 Thermal Plasma Monitor for Orbit 9380 on 29 Mar 1979 at a Time Coordinated With the Particle Precipitation Data of Figure 20

(Due to the large number of references cited above, they will not be listed here. See References, page 57.)

The rapid intensification of phase and amplitude scintillations in response to the particle precipitation and associated topside thermal density gradients raises important questions regarding the growth rate of the irregularities. It seems that a time scale of only a few minutes for the growth time is consistent with the observations. Such short linear growth times have recently been estimated for the gradient drift instability³⁹ in the auroral oval by Tsunoda and Vickrey.³⁸ These authors have also discussed the various complications that arise in the auroral oval when a conducting E-layer is present.⁴⁰ The present situation is similar as it is very likely that the low-energy precipitation zone which is embedded in the region of the diffuse aurora is associated with an eastward electrojet and possibly also downward field-aligned currents.⁴¹ It should be pointed out that the Goose Bay magnetogram (Figure 18b), taken at a location which is 5° north of the Fleetsat intersection point showed a 400γ negative bay, thereby implying a westward electrojet. The magnetometer studies of Harang⁴² clearly established that during the evening hours, eastward and westward currents could exist within the same longitude sector, the westward current being located furthest north. Further, the particle precipitation characteristics shown by DMSP in Figure 20 is consistent with our hypothesis that the westward electrojet was flowing at ~65°Λ whereas an eastward electrojet was probably flowing somewhere in the vicinity of 60°Λ. Thus the effect of conductivity and field-aligned currents⁴³ must also be considered in the general expression of the growth rate. Further, the long life time of the F-region density enhancements²⁷ and subsequent convection add to the problems of identifying locally generated irregularities from drifted structures. The current intense scintillation event under study, however, seems to be due to locally generated irregularities and a detailed theoretical study is underway⁴⁴ to identify specific plasma instability mechanisms which are consistent with the correlated data sets.

The encouraging results obtained from this case study merit further investigations on a statistical basis. A study has been initiated to determine from the DMSP data the frequency with which such low-energy electron precipitation is observed near the equatorward edge of the diffuse aurora and the geophysical conditions associated with these events.⁴⁵ We hope to utilize our near-continuous Goose Bay scintillation and TEC measurements to determine the effect of such precipitation events in the North Atlantic sector on transionospheric propagation.

(Due to the large number of references cited above, they will not be listed here. See References, page 57.)

Blank
56

References

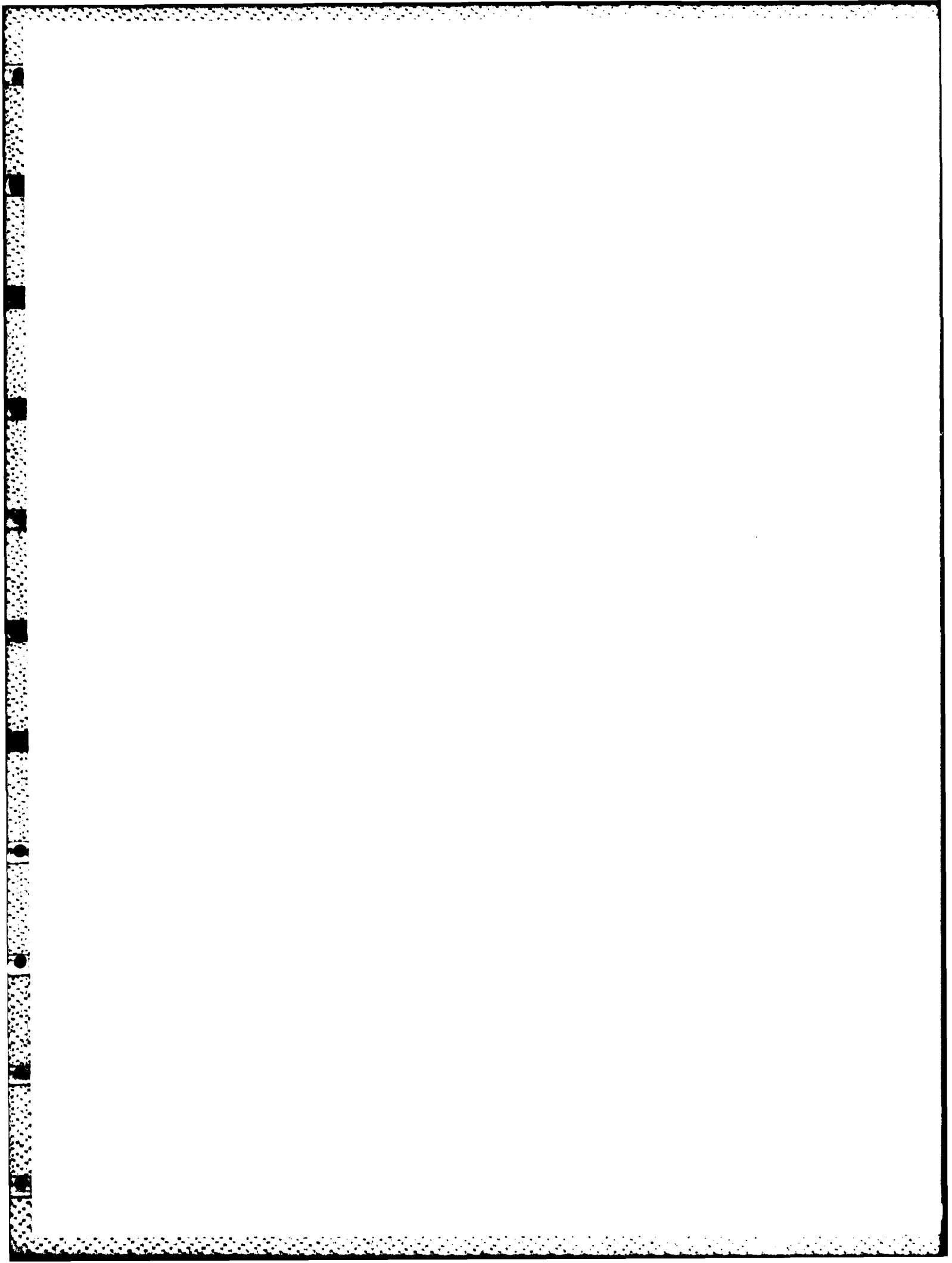
1. Basu, Sunanda, Basu, S., Livingston, R.C., Whitney, H.E., and MacKenzie, E. (1981) Comparison of Ionospheric Scintillation Statistics From the North Atlantic and Alaskan Sectors of the Auroral Oval Using the Wideband Satellite, AFGL-TR-81-0266, ADA111871.
2. Prettie, C.W. (1981) Phase Effects of Ionospheric Irregularities, AFWAL-TR-81-1163.
3. Basu, S., and Aarons, J. (1980) The morphology of high-latitude VHF scintillation near 70°W, Radio Sci. 15:59.
4. Feldstein, Y.I., and Starkov, G.V. (1967) Dynamics of auroral belt and polar geomagnetic disturbances, Planet. Space Sci. 15:209.
5. Whalen, J.A. (1970) Auroral Oval Plotter and Nomograph for Determining Corrected Geomagnetic Local Time, Latitude and Longitude for High Latitudes in the Northern Hemisphere, AFCRL-TR-70-0422, AD713170
6. McClure, J.P., and Hanson, W.B. (1973) A catalog of ionospheric F region irregularity behavior on Ogo-6 retarding potential analyzer data, J. Geophys. Res. 78:7431.
7. Basu, S. (1978) Ogo-6 observations of small scale irregularity structures associated with sub-trough density gradients, J. Geophys. Res. 83:182.
8. Fremouw, E.J., Leadabrand R.L., Livingston, R.C., Cousins, M.D., Rino, C.L., Fair, B.C., and Long, R.A. (1978) Early results from the DNA Wideband satellite experiment - complex-signal scintillation, Radio Sci. 13:167.
9. Livingston, R.C. (1980) Micro-Wideband Analysis Summary Output - Geosynchronous and Near-Synchronous Beacons, Technical Memorandum, SRI International, Menlo Park, California
10. Briggs, B.H., and Parkin, I.A. (1963) On the variation of radio star and satellite scintillations with zenith angle, J. Atmos. Terr. Phys. 25:339.
11. Rufenach, C.L. (1975) Ionospheric scintillation by a random phase screen: spectral approach, Radio Sci. 10:155.

References

12. Rino, C. L. (1979) A power law phase screen model for ionospheric scintillation. 1. Weak scatter, Radio Sci. 14:1135.
13. Houminer, Z., Aarons, J., and Rich, F. (1981) Production and dynamics of high-latitude irregularities during magnetic storms, J. Geophys. Res. 86:9939.
14. Smiddy, M., Kelley, M. C., Burke, W., Rich, F., Sagalyn, R., Shuman, B., Hays, R., and Lai, S. (1977) Intense poleward-directed electric fields near the ionospheric projection of the plasmapause, Geophys. Res. Lett. 4:543.
15. Wand, R. H., and Evans, J. V. (1981) The penetration of convection electric fields to the latitudes of Millstone Hill ($\Lambda = 56^\circ$), J. Geophys. Res. 86:5809.
16. Herman, J. R. (1966) Spread-F and ionospheric F region irregularities, Rev. Geophys. 4:255.
17. Aarons, J., Mullen, J., and Basu, Sunanda (1963) Geomagnetic control of satellite scintillation, J. Geophys. Res. 68:3159.
18. Frihagen, J. (1969) Satellite scintillation at high latitude and its possible relation to precipitation of soft particles, J. Atmos. Terr. Phys. 31:81.
19. Weber, E. J., and Buchau, J. (1981) Polar cap F-layer auroras, Geophys. Res. Lett. 8:125.
20. Martin, E., and Aarons, J. (1977) F-layer scintillation and the aurora, J. Geophys. Res. 82:2717.
21. Aarons, J. (1976) High-latitude irregularities during the magnetic storm of October 31 to November 1, 1972, J. Geophys. Res. 81:661.
22. Meng, C. I. (1981) Magnetospheric and Geomagnetic Activity During the First Year (1979) of the SCATHA (P78-2) Satellite Operation, Final Report, Contract MIPR FY71218000009, The Johns Hopkins University, AFGL-TR-81-0104, ADA104109.
23. Hardy, D. A., Gussenhoven, M. S., and Huber, A. (1979) The Precipitation Electron Detectors (SSJ/3) for the Block 5D/Flights 2-5 DMSP Satellites: Calibration and Data Presentation, AFGL-TR-79-0210, ADA083136.
24. Tanskanen, P. J., Hardy, D. A., and Burke, W. J. (1981) Spectral characteristics of precipitating electrons associated with visible aurora in the premidnight oval during periods of substorm activity, J. Geophys. Res. 86:1379-1395.
25. Gussenhoven, M. S., Hardy, D. A., and Burke, W. J. (1981) DMSP/F2 electron observations of equatorward auroral boundaries and their relationship to magnetospheric electric fields, J. Geophys. Res. 86:768.
26. Vickrey, J. F., Rino, C. L., and Potemra, T. A. (1980) Chatanika Triad observations of unstable ionization enhancements in the auroral F-region, Geophys. Res. Lett. 7:789.
27. Roble, R. G., and Rees, M. H. (1977) Time-dependent studies of the aurora: effects of particle precipitation on the dynamic morphology of ionospheric and atmospheric properties, Planet. Space Sci. 25:991.
28. Watkins, B. J., and Richards, P. G. (1979) A theoretical investigation of the role of neutral winds and particle precipitation in the formation of the auroral F-region ionosphere, J. Atmos. Terr. Phys. 41:179.
29. Fremouw, E. J. (1980) Geometrical control of the ratio of intensity and phase scintillation indices, J. Atmos. Terr. Phys. 42:775.

References

30. Foster, J. C., Doupnik, J. R., and Stiles, G. S. (1981) Ionospheric convection and currents in the midnight sector on November 8, 1979, J. Geophys. Res. 86:2143.
31. Rino, C. L., Tsunoda, R. T., Petricek, J., Livingston, R. C., Kelley, M. C., and Baker, K. D. (1981) Simultaneous rocket-borne beacon and in-situ measurements of equatorial spread-F - Intermediate wavelength results, J. Geophys. Res. 86:2411.
32. Basu, Sunanda, Basu, S., McClure, J. P., Hanson, W. B., and Whitney, H. E. (1982) High resolution topside in-situ data of electron densities and VHF/GHz scintillations in the equatorial region, J. Geophys. Res. (in press).
33. Keskinen, M. J., and Ossakow, S. L. (1982) Nonlinear evolution of plasma enhancements in the auroral ionosphere, 1: Long wavelength irregularities, J. Geophys. Res. 87:144.
34. Buchau, J., Aarons, J., Mullen, J. P., Weber, E. J., Whalen, J. A., Whitney, H. E., and Crampton, E. E. (1978) Amplitude scintillation studies in the polar region on 250 MHz, Paper presented at the Symposium on the Effect of the Ionosphere on Space and Terrestrial Systems, Arlington, Virginia, Jan. 1978, (AFGL-TR-78-0226, ADA059864).
35. Smiddy, M., Sagalyn, R. C., Sullivan, W. P., Wildman, P. J. L., Anderson, P., and Rich, F. (1978) The Topside Ionosphere Plasma Monitor (SSIE) for the Block 5D/Flight 2 DMSP Satellite, AFGL-TR-78-0071, ADA058503).
36. Rich, F. J. (1982) private communication.
37. Rino, C. L., and Vickrey, J. F. (1982) Recent results in the auroral zone scintillation studies, Accepted for publication in Radio Sci.
38. Tsunoda, R. T., and Vickrey, J. F. (1982) Evidence of east-west structure in large-scale F-region plasma enhancements in the auroral zone, Submitted to J. Geophys. Res.
39. Linson, L. M., and Workman, J. B. (1970) Formation of striations in ionospheric plasma clouds, J. Geophys. Res. 75:3211.
40. Vickrey, J. F., and Kelley, M. C. (1982) The effects of a conducting E layer on classical F-region cross-field plasma diffusion, J. Geophys. Res. 87:4461.
41. Kamide, Y., Murphree, J. S., Anger, C. D., Berkey, F. T., and Potemra, T. A. (1979) Nearly simultaneous observations of field-aligned currents and visible auroras by the Triad and ISIS-2 satellites, J. Geophys. Res. 84:4425.
42. Harang, L. (1946) Polar geomagnetic storms, J. Geophys. Res. 51:353.
43. Ossakow, S. L., and Chaturvedi, P. K. (1979) Current convective instability in the diffuse aurora, Geophys. Res. Lett. 6:322.
44. Lee, M. C., Basu, Sunanda, and Basu, S. (1982) Gravitational instabilities as the causes of high-latitude kilometer-scale ionospheric irregularities Submitted to Geophys. Res. Lett.
45. Hardy, D. A. (1982) private communication.



DNA Distribution List

Berkeley Research Assoc.
Attn: Clifford W. Prettie
P.O. Box 983
Berkeley, CA 94701

ESL, Inc.
Attn: J. Marshall
495 Java Drive
Sunnyvale, CA 94086

Def. Nuclear Agency
Attn: STTL Tech. Library
Washington, D. C. 20305

Mission Research Corp.
Attn: R. Bogush
735 State St.
Santa Barbara, CA 93101

Naval Research Lab.
Attn: Dr. John Goodman
Code 4110
Washington, D. C. 20375

Dr. J. Aarons
Boston University
Boston, MA 02215

Major G. Wortham
AFGWC/WSE
Offutt AFB, NE 68113

Lt. P. Styczek
SACCA/CSS
Offutt AFB, NE 68113

Ed Skomal
Aerospace Corp.
Box 92957
Los Angeles, CA 90009

Allen L. Johnson
Air Force Avionics Lab
AFAL/AAAI
Wright Patterson AFB
Ohio 45433

Dow Evelyn
Def Nuclear Agency/RAAE
Washington, D. C. 20305

Major L. Wittwer
Def Nuclear Agency/RAAE
Washington, D. C. 20305

Major R. Sutton
SD/YKX
P.O. Box 92960
Worldway Postal Center
Los Angeles, CA 90009

Dr. H. Soicher
US Army Communication Res. and
Development Commons
Fort Monmouth, NJ 07703
(DRDCO-COM-RH-4)

SRI International
333 Ravenswood Ave.
Menlo Park, CA 94025
Attn: C. Rino

SRI International
333 Ravenswood Ave.
Menlo Park, CA 94025
Attn: R. Livingston

Physical Dynamics, Inc.
P.O. Box 3027
Bellevue, WA 98009
Attn: E.J. Fremouw

Dr. K. Davies
NOAA
Boulder, CO 80302

Dr. H. Mullaney
Code 427
Dept. of the Navy
Office of Naval Research
Arlington, VA 22217

Dr. George Millman
General Electric Co.
Building 9, Room 46
Court Street Plant
Syracuse, NY 13201

Prof. K.C. Yeh
University of Illinois
Dept. of Electric Engineering
Urbana, IL 61801

Dr. Warren Brown
Sandia Lab
ORG 314
Albuquerque, NM 87185

Dr. C.H. Liu
60 Electrical Engineering Building
University of Illinois
Urbana, IL 61801

Dr. S. Ossakow
Plasma Dynamics, Code 7750
U.S. Naval Research Lab
Washington, D.C. 20390

Dr. Phil McClure
U. of Texas at Dallas
Richardson, TX 75080

Prof. H.G. Booker
Dept. of Applied Physics
U. of Calif. at San Diego
La Jolla, CA 92037

Prof. Michael Kelley
Dept. of Elect. Engineering
Cornell University
Ithaca, NY 14850

Prof. W.B. Hanson
U. of Texas at Dallas
Richardson, TX 75080